Runoff from Greenland's firn area – why do MODIS, RCMs and a firn model disagree?

Horst Machguth[1], Andrew Tedstone[1, *], Peter Kuipers Munneke[2], Max Brils[2, **], Brice Noël[3], Nicole Clerx[1, ***], Nicolas Jullien[1], Xavier Fettweis[3], and Michiel van den Broeke[2]

[1]Department of Geosciences, University of Fribourg, Fribourg, Switzerland
[2]Institute for Marine and Atmospheric research Utrecht, Utrecht University, Utrecht, Netherlands
[3]Laboratory of Climatology, Department of Geography, SPHERES research unit, University of Liège, Liège, Belgium
[*]Now at Institute of Earth Surface Dynamics, University of Lausanne, Lausanne, Switzerland
[**]Now at Geography and Environmental Sciences Department, Northumbria University, Newcastle, United Kingdom
[***]Now at Environmental Remote Sensing Laboratory, EPFL, Lausanne, Switzerland

Correspondence: Horst Machguth (horst.machguth@unifr.ch)

Abstract. Due to increasing air temperatures, surface melt and meltwater runoff expand to ever higher elevations on the Greenland ice sheet and reach far into its firn area. Here, we evaluate how two regional climate models (RCMs) simulate the expansion of the ice sheet runoff area: MAR, and RACMO with its offline firn model IMAU-FDM. For the purpose of this comparison we first improve an existing algorithm to detect daily visible runoff limits from MODIS satellite imagery. We then apply the improved algorithm to most of the Greenland ice sheet and compare MODIS to RCM runoff limits for the years 2000 to 2021. We find that RACMO/IMAU-FDM runoff limits are on average somewhat lower than MODIS and show little fluctuations from year to year. MAR runoff limits are substantially higher than MODIS, but their relative fluctuations are more similar to MODIS. Both models apply a bucket scheme where meltwater is routed vertically. On the example of the K-transect we demonstrate that differences in the implementation of the bucket scheme are responsible for the disparity in RCM simulated runoff limits. The formulation of the runoff condition is of large influence: in RACMO/IMAU-FDM meltwater is only considered runoff when it reaches the bottom of the simulated firn pack; in MAR runoff can also occur from within the firn pack, which largely causes its higher runoff limits. We show that total runoff along the K-transect, simulated by the two RCMs, diverges by up to 29 % in extraordinary melt years. Out of this, three quarters are caused by the differences in the simulated runoff limits, the remainder being mostly due to differences in simulated ablation area runoff. Consequently, accurate simulation of meltwater hydrology in a melting firn area is essential to assess Greenland's current and future mass changes.

1 Introduction

Polar regional climate models (RCMs) are our most advanced tools to assess past, present and future surface mass balance of the Greenland and Antarctic ice sheets (Box et al., 2004; Fettweis et al., 2008; Noël et al., 2016; IMBIE Team, 2018, 2020). The accuracy of RCM output relies, among other factors, on data available for model calibration and evaluation. Essential for RCM evaluation are meteorological observations (e.g. Steffen and Box, 2001; Fausto et al., 2021), surface mass balance

measurements (e.g. Benson, 1962; Greuell et al., 2001; van de Berg et al., 2006; Machguth et al., 2016b; Karlsson et al., 2016; Fausto et al., 2021) and remote sensing products (e.g. Fettweis et al., 2006; Mohajerani et al., 2019; Slater et al., 2021). RCMs have been extensively evaluated for Greenland's ablation area (e.g. Gallee and Duynkerke, 1997; Lefebre et al., 2005; Noël

25 et al., 2016) and its higher accumulation area (e.g. Rae et al., 2012; Noël et al., 2016) and have been found to perform well (e.g. Fettweis et al., 2017, 2020). However, advanced model evaluation requires also testing the RCMs in the transition zone in-between the ablation and the higher accumulation area. In this area a delicate balance exists between accumulation and ablation processes. In summer, when melt, runoff and accumulation can occur simultaneously, working conditions are challenging (e.g. Holmes, 1955; Clerx et al., 2022). Consequently, the availability of field data is limited and few studies (e.g. Covi et al., 2022;

30 Zhang et al., 2023) evaluated RCMs in that transition zone.

Within the elevation range of the transition zone lie the equilibrium line altitude (ELA) and the runoff limit. The former is the elevation which separates accumulation and ablation areas, the latter is defined as the uppermost elevation from where meltwater can reach the ocean and contribute to mass loss (Cogley et al., 2011; Tedstone and Machguth, 2022; Clerx et al., 2022). The runoff limit lies within the accumulation area (Shumskii, 1955, 1964), and is thus located *above* the ELA. The

35 ELA in combination with the ice sheet hypsometry determines the ratio of accumulation to ablation area, while the elevation of the runoff limit defines the ice sheet surface area over which mass loss takes place. Any shift in ELA and/or the runoff limit impacts the surface mass balance of the ice sheet.

Tedstone and Machguth (2022) compared seasonal maxima of visible runoff limits, mapped from Landsat satellite imagery, to runoff extent simulated by the two RCMs RACMO 2.3p2 (Noël et al., 2018) and MAR v3.11 (Fettweis et al., 2017) forced

40 by ERA-40/ERA-I/ERA5. The comparison revealed substantial differences between RCMs and remotely sensed runoff limits, but also between the two RCMs involved. While remotely sensed runoff limits are subject to uncertainties, it remains unclear what causes the remarkable differences between the RCMs. If RCMs differ strongly in simulating the area of the Greenland ice sheet that contributes to sea level change, this could also indicate inaccuracies in future scenarios of runoff area, mass loss and sea-level contribution.

45 Here we aim at explaining these differences. We compare remotely sensed runoff limits to RACMO and MAR, and also directly oppose the runoff limits simulated by the two RCMs. Instead of seasonal maxima from Landsat, we use daily Moderate Resolution Imaging Spectroradiometer (MODIS) runoff limits for the years 2000 to 2021. derived by an improved version of the algorithm used in Machguth et al. (2022). We analyze the differences between MODIS, MAR and RACMO runoff limits in the context of RCM-simulated parameters that potentially influence simulated runoff. Among the selected parameters are surface

50 albedo, firn density and temperature, as well as refreezing. We point out which of the parameterizations in the RCMs likely cause the deviations. Finally, we quantify their impact on simulated mass balance along a transect in south-west Greenland.

2   Data

2.1   Data for MODIS runoff limit detection

The detection of MODIS runoff limits Υ_{obs} is based on an optimized version of the algorithm by Machguth et al. (2022). The
55   improved algorithm (Sec. 3.1) relies on the following input: (i) daily MOD10A1 data (MODIS/Terra Daily Snow Cover at
500 m resolution, version 6.0; Hall and Riggs, 2016); (ii) daily MOD09GA data (MODIS/Terra Surface Reflectance Daily at
500 m, version 6.0; Vermote and Wolfe, 2015); (iii) the Arctic DEM (100 m resolution mosaic, v.3.0; Porter et al., 2018, here
downsampled to the 500 m MODIS grid); (iv) outlines of the Greenland ice sheet according to Rastner et al. (2012) and (v)
Greenland-wide arrays of surface ice flow velocity in x and y direction (Joughin et al., 2016, 2017).

60   ### 2.2   RCM data

To quantify RCM modelled runoff limits Υ_{rcm} we use (i) simulated runoff from the polar regional climate model MAR (version
3.14, 10 km resolution, forced by ERA5, see Section 3.2.1), (ii) the polar version of the Regional Atmospheric Climate Model
RACMO (Noël et al., 2019, version 2.3p2 on the grid FGRN055, forced by ERA5) at a resolution of 5.5 km as well as (iii) the
offline firn model IMAU-FDM v1.2G (Ligtenberg et al., 2011, 2018; Brils et al., 2022). RACMO data are frequently used in a
65   version that is further downscaled to 1 km resolution and bias corrected (Noël et al., 2016; Noël et al., 2019). The downscaled
data have a temporal resolution of 1 day, which is insufficient to force IMAU-FDM v1.2G, so for firn applications these data
cannot be used. Nevertheless, as the 1 km data are frequently applied to assess Greenland mass balance we use them here for
basic comparison to the other models and MODIS.

   We use a set of RCM parameters (Table 1) to explore the reasons behind potential differences in MODIS and RCM runoff
70   limits. Various parameters are not available directly from RACMO2.3p2 and are instead obtained from the offline firn model
IMAU-FDM v1.2G henceforth IMAU-FDM. The model is forced in offline mode by RACMO2.3p2 and is run on an identical
spatial grid. In the following we refer to 'MAR' for MARv3.14, to 'RACMO' for RACMO2.3p2 at native resolution of 5.5 km
and we use 'RACMO 1 km' when we refer to downscaled and bias corrected RACMO2.3p2 data.

   MAR and RACMO 1 km data are obtained at daily temporal resolution. RACMO and IMAU-FDM are at 10-day intervals.
75   Where needed, MAR data are averaged or summed to the lower temporal resolution.

3   Methods

3.1   Detecting MODIS Υ_{obs} along flowlines

The algorithms by Greuell and Knap (2000) and Machguth et al. (2022) detect Υ_{obs} on relatively coarse resolution AVHRR
(1.1 km; Greuell and Knap, 2000) or MODIS (500 m; Machguth et al., 2022) satellite imagery. Given the low spatial resolution
80   as compared to e.g. Landsat, Υ_{obs} is identified indirectly, that is where spatial variability of surface albedo α transitions from
low to high. Low spatial variability of α indicates a monotonous snow covered surface. Variability of α is high where dark

Table 1. List of RCM simulated parameters used to calculate and investigate runoff limits. "RACMO 1 km" stands for RACMO2.3p2 downscaled to 1 km and bias corrected, "RACMO" stands for RACMO2.3p2 at native 5.5 km resolution, "IMAU-FDM" stands for IMAU-FDM v1.2G and "MAR" stands for MARv3.14.

Parameter	Source				Unit	Description
	RACMO 1 km	RACMO	IMAU-FDM	MAR		
fac_{10m}			x	x	m	Firn air content top 10 m
lwc_{1m}			x	x	kg	Liquid water content top 1 m
lwc_{tot}			x	x	kg	Liquid water content entire firn pack
R			x	x	mm w.e.	Refreezing
Q	x		x	x	mm w.e.	Runoff
T_{10m}			x	x	°C	Firn/ice temperature at 10 m depth
M		x		x	mm w.e.	Melt
α		x		x		Surface albedo
ρ			x	x	$\mathrm{kg\,m^{-3}}$	Density profile 0 to 20 m depth

meltwater streams, lakes and slush fields intersect the bright snow cover. Despite this indirect approach, MODIS Υ_{obs} highly agree to visible runoff limits detected on finer resolution (30 m) Landsat imagery (Machguth et al., 2022).

Machguth et al. (2022) scanned rectangular polygons of width p_w and length $p_l \gg p_w$ for the location where the standard deviation of surface albedo σ_α falls below a certain threshold. If a set of additional conditions and tests are fulfilled (see Machguth et al., 2022), the location is considered to represent Υ_{obs}. The long axes of the polygons needed to be oriented along the strongest gradient in α, which is in the direction of the surface slope. Polygons in Machguth et al. (2022) were strictly oriented west-east. Consequently, the application of the method was restricted to areas of the western flank of the ice sheet.

Here we apply the method by Machguth et al. (2022), summarized above, with two major modifications that allow application to all of the Greenland Ice Sheet: (1) We create so called flowline-polygons of $p_w = 20$ km, henceforth simply called flowlines, and (2) implement an improved calculation of σ_α. The former allows detection of Υ_{obs} in complex topography, the latter improves detections of Υ_{obs} by calculating and subtracting the influence of temporally persistent albedo features. These major modifications, as well as some smaller optimizations, are detailed in Appendix A. For further details on the algorithm we refer to Machguth et al. (2022).

3.2 RCM simulations of the firn cover and runoff

3.2.1 MAR

Here we use daily outputs at 10 km resolution from version 3.14 of MAR, forced every 6 hours by the ERA5 reanalysis. The MARv3.14 data used here are composed of two transient simulations: the first one starts in September 1974 but only the period 1980-1999 is used. The second one begins in September 1994 and the period 2000-2023 is used. Together, the two simulations

100   cover the years 1980 to 2023. In the set-up used here, MAR resolves the uppermost 21 m of snow and firn using a time-varying number of layers up to a maximum of 21 layers. For densities lower than $450\,\mathrm{kg\,m^{-3}}$, the CROCUS snow model albedo (Brun et al., 1992) is used with a minimum value of 0.7. Where snowpack is present but has a surface density higher than $450\,\mathrm{kg\,m^{-3}}$ (the maximum density of pure snow), then the minimum value of albedo declines between the minimum pure snow albedo (0.7) and clean ice albedo (0.55) as a linear function of increasing density. On bare ice (surface density higher than $900\,\mathrm{kg\,m^{-3}}$),

105   CROCUS snow model albedo is no more used and the albedo varies exponentially between 0.55 (clean ice) and 0.5 (dirty ice) as a function of the accumulated surface water height and the slope.

The main changes of MARv3.14 with respect to MARv3.12 (Vandecrux et al., 2024) are as follows: Some bugs in the clouds scheme have been corrected and a continuous snowfall-rainfall limit has been introduced for near-surface temperature between -1 °C (100 % of precipitation falls as snow) and +1 °C (100 % rain). MARv3.14 now uses the radiative scheme from ERA5

110   (Hogan and Bozzo, 2018) instead of the one from ERA40 (Morcrette, 2002) in former MAR versions. The maximum liquid water content in the snow and firn (i.e. irreducible water saturation) is 7 % at the surface and linearly reduces to 2 % at 1 m depth. Below that depth, irreducible water saturation is set to 2 %. Slush is not allowed in these MARv3.14 simulations; if the density of a layer is $<830\,\mathrm{kg\,m^{-3}}$, percolation to the next deeper layer starts as soon as irreducible water saturation is reached. For layers of density $\geq 830\,\mathrm{kg\,m^{-3}}$, a density runoff threshold determines how much of any excess meltwater gets removed

115   immediately as runoff: 0 % for $830\,\mathrm{kg\,m^{-3}}$ to 100 % for densities above $900\,\mathrm{kg\,m^{-3}}$. The remainder percolates to the next layer below. Where ice lenses are simulated by MAR, 2/3 of the percolating meltwater progress to underlying layers and the remaining 1/3 are considered run off. Thereby an ice lens is defined as a layer with a density of $>900\,\mathrm{kg\,m^{-3}}$ that lies on top of a layer where density is $\leq 900\,\mathrm{kg\,m^{-3}}$.

For further details on MAR we refer to Fettweis et al. (2013, 2017, 2020). Previous MAR versions have been successfully

120   validated over the Greenland ice sheet by comparison with surface mass balance measurements (Fettweis et al., 2020), satellite derived melt extent (Fettweis et al., 2011) and *in situ* atmospheric measurements (Delhasse et al., 2020).

3.2.2   IMAU-FDM and RACMO

IMAU-FDM v1.2G (Brils et al., 2022) is a semi-empirical firn densification model that simulates the time evolution of firn density, temperature, liquid water content and changes in surface elevation owing to variability of firn depth . Vertical water

125   transport in IMAU-FDM is instantaneous and calculated via the bucket method. In the absence of refreezing, only irreducible water is retained following Coléou and Lesaffre (1998) (e.g. 13 % irreducible water at a snow density of $300\,\mathrm{kg\,m^{-3}}$, 2.4 % at $800\,\mathrm{kg\,m^{-3}}$). When the water reaches the interface between firn and glacial ice, it is assumed to instantaneously run off. The depth of the horizontal modelling domain of IMAU-FDM varies in space and time and is defined by the condition that the deepest 200 grid cells must all exceed a density of $910\,\mathrm{kg\,m^{-3}}$. The thickness of the firn layer, that is from the surface to the

130   depth below which all grid cells exceed a density of $830\,\mathrm{kg\,m^{-3}}$, also varies and reaches maxima of 100 m in high-accumulation regions of the south-east of the ice sheet. A more typical maximum firn thickness is $\sim 70\,\mathrm{m}$.

IMAU-FDM is forced at the upper boundary by 3-hourly RACMO surface temperature and mass fluxes, interpolated to 15 minutes. RACMO's firn layer uses similar physical parametrisations as IMAU-FDM, but with a lower vertical resolu-

tion (max. 150 vs. 3000 layers) and less comprehensive initialisation to save computing costs. In RACMO, the snow albedo

135 scheme is based on prognostic snow grain size, cloud optical thickness, solar zenith angle and impurity concentration in snow (Kuipers Munneke et al., 2011). Impurity concentration is assumed constant in time and space. Bare ice albedo is prescribed from the 500 m MODIS 16-day albedo version 5 product (MCD43A3v5) as the lowest 5 % surface albedo records for the period 2000–2015. Thresholds are applied to these values: minimum ice albedo is set to 0.30 for dark ice in the low-lying ablation zone, and a maximum value of 0.55 is used for bright ice under perennial snow cover in the accumulation zone, i.e. only used

140 when all firn melts away which does not happen in this run. RACMO snow albedo typically ranges between ∼0.7 for highly metamorphosed, coarse grained snow under clear-sky conditions and ∼0.95 for fine grained snow under cloudy conditions. RACMO2.3p2 surface energy balance, surface mass balance and melt output over the GrIS have been extensively evaluated, notably along the K-transect, and were found to be generally robust (Noël et al., 2019).

The RACMO 1 km data are a statistically downscaled and bias corrected version of the RACMO2.3p2 data (Noël et al.,

145 2019). Here we use only RACMO 1 km runoff which differs from the original RACMO data due to (i) an albedo bias correction, being applied only in the bare ice zone, and (ii) an elevation gradient correction (Noël et al., 2016; Noël et al., 2019). For details on downscaling and bias correction we refer to the aforementioned sources.

3.3 Calculating Υ_{rcm} from RCM output

We distinguish between daily runoff limits Υ_{rcm} and annual maximum runoff limits $\max\Upsilon_{\mathrm{rcm}}$. Both are calculated on the

150 same 20 km wide flowlines as used for the detection of Υ_{obs}. For each flowline, we consider RCM grid cells whose center falls within the flowline. Given the elevation of each grid cell and simulated runoff, we then calculate runoff against elevation. There is no generally accepted definition of $\max\Upsilon_{\mathrm{rcm}}$. We explored different thresholds, namely >1, >5, >10, >20 and >100 mm w.e. of runoff per year. We found that the position (elevation) of $\max\Upsilon_{\mathrm{rcm}}$ for both RCMs is rather insensitive to the chosen runoff thresholds (see also Tedstone and Machguth, 2022). Hence, for the remainder of the study we calculate $\max\Upsilon_{\mathrm{rcm}}$ using a

155 threshold of >10 mm w.e. of runoff per year. To calculate daily Υ_{rcm} we adopt a threshold of >1 mm w.e. day^{-1}.

3.4 Analyzing RCM process simulations near the runoff limit

Our goal is to understand why deviations occur (i) between Υ_{obs} and Υ_{rcm} and (ii) between the two Υ_{rcm}. We focus this part of the analysis on the K-transect which has been studied intensively with respect to ice sheet boundary layer meteorology (van den Broeke et al., 1994), surface mass balance (Van de Wal et al., 2005, 2012), firn processes (Machguth et al., 2016a; Mikkelsen

160 et al., 2016; Rennermalm et al., 2021) and firn hydrology (Clerx et al., 2022). Here we defined the K-transect as the line that follows the 67 °N parallel, starts at the ice margin at ∼250 m a.s.l. / 50 °W, and reaches to the ice divide at ∼2520 m a.s.l. / 42.7 °W (Fig. 1). For both RCMs and IMAU-FDM, we extract the grid cells which are closest to the ∼320 km long transect. This results in lines of RCM grid cells which are one cell wide and 33 (MAR) or 57 cells (RACMO, IMAU-FDM) in length.

Along the K-transect we analyse the RCM simulated parameters listed in Table 1. We quantify temporal and spatial changes

165 and search for parameters that show peculiar or unexpected values in the broader elevation range around the runoff limit. If found, we investigate the underlying RCM parameterizations in order to understand their potential influence on Υ_{rcm}.

4 Results

4.1 MODIS Υ_{obs} detections

Figure 1 summarizes the resulting MODIS-derived Υ_{obs} for all of the Greenland Ice Sheet. The approach creates few and
170   meaningless Υ_{obs} in areas dominated by meltwater discharge through aquifers. This is to be expected as surface meltwater
features are largely absent in such areas. Consequently we masked all retrievals from 60 to 68.4 °N along Greenland's east
coast. We did not mask detected Υ_{obs} located in smaller aquifer regions elsewhere on the ice sheet. After masking, 63,400
Υ_{obs} in 417 flowlines remain, which corresponds on average to ~7 retrievals per flowline and year. The actual number of
annual retrievals varies geographically and is highest in the southwest, exceeding on average 18 retrievals per flowline and
175   melt season.

      Compared to Machguth et al. (2022) and their study area, we find that the updated algorithm yields ~80 % more Υ_{obs}
detections. This difference is mainly due to the new algorithm being able to place more flowlines that are optimized for
complex topographies. The number of Υ_{obs} detections per flowline is 5.5 % higher than per stripe, which were the strictly east-
west oriented bands in Machguth et al. (2022). Outside of the area investigated by Machguth et al. (2022), the new approach
180   provides numerous detections of Υ_{obs} in the north-west of Greenland, from near Thule to Humboldt and Petermann glaciers,
as well as in the region of the north-east Greenland ice stream. Few detections occur along the central part of the east coast
where the terrain is complex and steep, with outlet glaciers that are narrow compared to the 20 km width of the flowlines. The
approach appears not well suited to such terrain. Apart from Petermann Glacier, there are few detections beyond 80 °N, the
reasons for which are unclear. Tedstone and Machguth (2022), who used Landsat to detect surface hydrology, also noted few
185   detections in the region.

      Figures 2, A1 and A2 exemplify the temporal detail of the Υ_{obs} data. The examples in Fig. 2 demonstrate frequent behavior
where Υ_{obs} rises relatively early in the melt season and reaches a plateau before melting ends (see also Machguth et al., 2022).
By design of the detection and filtering algorithms, there is typically no decrease in Υ_{obs} towards the end of the melt season:
Most decreasing Υ_{obs} are filtered out because optical remote sensing is poorly suited to detect continued hydrological activity
190   under freshly fallen autumn snow (Machguth et al., 2022).

4.2 Comparing Υ_{obs} and Υ_{rcm}

4.2.1 Comparing annual maxima

Figure 3 shows how $\max\Upsilon_{\mathrm{obs}}$ and $\max\Upsilon_{\mathrm{rcm}}$ vary along Greenland's western flank. The RCMs and MODIS show a general
decrease of the runoff limit towards higher latitudes (Fig. 3b). Certain deviations from this trend are common to all data:
195     $\max\Upsilon_{\mathrm{obs}}$ and $\max\Upsilon_{\mathrm{rcm}}$ are depressed south of ~63 °N and elevated in-between ~71 °N and ~72.5 °N. Where firn aquifers
are present MODIS $\max\Upsilon_{\mathrm{obs}}$ are biased low and standard deviation of $\max\Upsilon_{\mathrm{obs}}$ is increased. Otherwise, the differences
between $\max\Upsilon_{\mathrm{obs}}$ and $\max\Upsilon_{\mathrm{rcm}}$ depend strongly on the RCM. IMAU-FDM simulated runoff limits are mostly lower than
$\max\Upsilon_{\mathrm{obs}}$ and they have low standard deviation in comparison to MODIS. The downscaled and bias corrected RACMO 1 km

data show $\max\Upsilon_{\mathrm{rcm}}$ similar to MODIS but with the same small standard deviation as IMAU-FDM. MAR $\max\Upsilon_{\mathrm{rcm}}$ and its
200   standard deviation are substantially higher than MODIS. The difference is highest in the southwest and decreases towards the
north.

Figure 4 illustrates for two selected regions how the same parameters fluctuate over time. IMAU-FDM and RACMO 1 km
simulated runoff limits vary little between the years. The intense melt seasons of 2012 and 2019 leave virtually no trace in
their runoff limits. MAR $\max\Upsilon_{\mathrm{rcm}}$ vary with the intensity of the melt season. Temporal variability of MAR $\max\Upsilon_{\mathrm{rcm}}$ exceeds
205   MODIS in the south (Fig. 4b), but is rather similar further north (Fig. 4a).

4.2.2   Comparing seasonal evolution of Υ_{obs} and Υ_{rcm}

When comparing the seasonal evolution of Υ_{rcm} and Υ_{obs} we find that MODIS and RCM runoff limits similarly reach a plateau
before melt ceases (Figs. 2, A1 and A2). The plateau is shorter in the north than in the south. The date of the first appearance
of the runoff limit is mostly similar between RCMs and MODIS. Also the end of the plateau is similar between MODIS and
210   RCMs: There are very few cases where MODIS retrievals end but RCMs continue to see the runoff limit at $\max\Upsilon_{\mathrm{rcm}}$, there is
no case where the RCMs simulate an autumnal drop but MODIS continues detecting Υ_{obs} at peak elevation.

Agreement of IMAU-FDM to MODIS seasonal evolution is generally good (Figs. 2, A1 and A2). However, IMAU-FDM
Υ_{rcm} always tends to plateau at very similar elevations, regardless of the intensity of the melt season. This is the same behavior
shown for $\max\Upsilon_{\mathrm{rcm}}$ in Fig. 4. MAR simulated runoff limits typically increase fast in the early season and overshoot MODIS
215   (Figs. A1 and A2). However, Figs. 2 and 4 demonstrate that there are years and flowlines where MAR Υ_{rcm} is lower than
RACMO and in good agreement with MODIS Υ_{obs}.

The rise of the runoff limit appears more step-wise in the RCMs and more gradual in the MODIS data. However, this
impression might also be partially related to the different temporal resolution of RCM and MODIS data. During the melt
seasons, Υ_{rcm} can fluctuate strongly, often dropping and increasing, within a few days, over hundreds of meters in elevation
220   (e.g. Fig. 2). MODIS Υ_{obs} indicate a more continuous process where the visible runoff limit remains at high elevations, also
during cold spells.

4.3   RCM process simulations at the runoff limit

The comparison reveals large differences between Υ_{rcm} simulated by MAR and IMAU-FDM. We focus on the K-transect
to explore reasons behind the deviations. Figures 5 and 6 visualize and compare RCM simulated parameters for the two
225   contrasting melt seasons of 2012 and 2017. The former was dominated by early, persistent and intense melting, the latter by
intermittent and moderate melt. They represent the end members of the last 25 mass balance years that were dominated by
mass loss.

In 2012, IMAU-FDM shows discontinuities at the location of $\max\Upsilon_{\mathrm{rcm}}$: Mean albedo increases by $\sim$0.05 (Fig. 5c) while
melt drops by $\sim$400 mm w.e. or 31 % (Fig. 5e). The contrast in albedo is even higher (an increase from 0.65 to 0.78) when
230   averaging only from mid-July to mid-August 2012. At $\max\Upsilon_{\mathrm{rcm}}$, runoff drops from slightly higher than 1000 mm w.e. to zero
(Fig. 5e). While $\sim$80 % of melt runs off at $\max\Upsilon_{\mathrm{rcm}}$, the runoff fraction immediately falls to zero above (Fig. 5g). This sudden

shut-down of runoff is compensated by an abrupt increase in refreezing (Figs. 5i). In 2012 all these transitions take place over the distance of a single grid cell (5.5 km), whereas in 2017, IMAU-FDM shows gradual transitions without discontinuities (Fig. 5d, f, h and k). In 2012, MAR shows no discontinuities in albedo and melt across $\max\Upsilon_{\mathrm{rcm}}$ (Figs. 5c and e) but it exhibits

235 step-wise changes in runoff and refreezing (Fig. 5g and i). These discontinuities are somewhat less pronounced than for IMAU-FDM. In 2017, simulated refreezing of MAR and IMAU-FDM are rather similar along the transect (Fig. 5k), regardless of MAR $\max\Upsilon_{\mathrm{rcm}}$ being located at higher elevation.

In 2012, IMAU-FDM Υ_{rcm} remained stable over an extended time period (e.g. Fig. 6c). The sharp increase in total refreezing, observed in Fig. 5i, is the result of intense refreezing that took place, over the prolonged time period when the IMAU-FDM

240 runoff limit was at its maximum (Fig. 6e). The refreezing raised 10 m firn temperatures to $0\,^{\circ}\mathrm{C}$ (Fig. 6g), which is unique for the decade 2010 to 2020 (Fig. A3). In 2012, MAR refreezing was also focused to directly above Υ_{rcm} (Fig. 6l), but not as clearly as IMAU-FDM. The peak in MAR summed refreezing is thus less pronounced (Fig. 5i). We notice that MAR refreezing fluctuates somewhat randomly along the transect. These fluctuations can be observed in both years and occur mainly in-between the $\max\Upsilon_{\mathrm{rcm}}$ of the two RCMs (Figs. 5i, k). The fluctuations can also be seen in Figs. 6l and m.

245 In MAR, there is less influence of refreezing on 10 m firn temperatures (Fig. 6n and o). Firn temperatures below the 2012 $\max\Upsilon_{\mathrm{rcm}}$ were already very close to zero and thus could not warm further. The relatively intense 2012 refreezing results in moderate firn warming above $\max\Upsilon_{\mathrm{rcm}}$ which then persists (Fig. A3).

Figure 7 serves to assess whether $\max\Upsilon_{\mathrm{rcm}}$ are related to simulated firn structure. In 2012, IMAU-FDM $\max\Upsilon_{\mathrm{rcm}}$ coincides with the uppermost grid cell where the top 20 m of the firn consist of ice. MAR $\max\Upsilon_{\mathrm{rcm}}$ is underlain by less dense firn and

250 is located much higher than the uppermost grid cell of uniform ice. Furthermore, we notice that the IMAU-FDM firn profile shows an ice slab, a zone of icy firn in the top ~ 5 m of the firn profile overlying material of lower density. The slab is most pronounced directly uphill of the 2012 IMAU-FDM $\max\Upsilon_{\mathrm{rcm}}$. The MAR firn profiles shows only a weakly developed zone of increased near-surface density above the 2012 MAR $\max\Upsilon_{\mathrm{rcm}}$, but it features a zone of high density below ~ 12 m depth directly adjacent of the zone of uniform glacier ice. At high elevations, roughly above MAR $\max\Upsilon_{\mathrm{rcm}}$, MAR simulated firn

255 density is mostly lower than for IMAU-FDM.

We visualize firn density evolution over the time period 1980-2020 at the KAN_U site, located at 1840 m a.s.l. on the K-transect (Fig. 8). The site has a unique record of firn density measurements that show ice slab evolution since 2012 (Rennermalm et al., 2021). Figure 8 shows the top 20 m of the simulated firn which corresponds to all firn layers simulated in MAR. IMAU-FDM simulated firn depth at KAN_U is on average 53 ± 1 m. IMAU-FDM firn density evolution shows annual

260 layers getting buried and an ice slab forming in summer 2012. The slab, also visible in Fig. 7, gets afterwards buried under accumulating snow and firn. Both IMAU-FDM and MAR show a general trend towards increasing firn density. However, MAR simulates a higher firn density at the KAN_U site ($624\,\mathrm{kg\,m^{-3}}$ vs. $771\,\mathrm{kg\,m^{-3}}$) and the coarser vertical resolution of the MAR outputs makes it more difficult to follow horizons as they get buried.

4.4 Υ_{rcm} and its relevance for RCM simulated runoff

265 The difference between the two $\max\Upsilon_{\mathrm{rcm}}$ is larger in the very intense 2012 melt year than during the moderate 2017 melt season (Figs. 5 and 6). MAR simulates runoff between the two runoff limits, and the question arises to what degree this is relevant to overall runoff. On the example of the K-transect we quantify by how much total simulated runoff is influenced by differences in IMAU-FDM and MAR $\max\Upsilon_{\mathrm{rcm}}$.

For each year from 1980 to 2020 we calculate total annual RCM runoff (i) below and (ii) above IMAU-FDM $\max\Upsilon_{\mathrm{rcm}}$
270 along the K-transect (see the inset in Fig. 9). The first value, termed $\int_{\Downarrow} Q$, can be calculated from both RCMs. The second value, $\int_{\Uparrow} Q$, can only be calculated from MAR whose $\max\Upsilon_{\mathrm{rcm}}$ is always higher than IMAU-FDM along the K-transect.

Exponential regression of the two parameters $\int_{\Downarrow} Q_{\mathrm{MAR}}$ and $\int_{\Uparrow} Q_{\mathrm{MAR}}$ yields $R^2 = 0.83$ (Fig. 9), which means the more intense the melt season, the larger the difference in total runoff simulated by the two RCMs. The exponential regression curve indicates that runoff from above IMAU-FDM $\max\Upsilon_{\mathrm{rcm}}$ grows disproportionately with melt season intensity. The reason for the
275 disproportional growth is that the more intense the melt season, the further apart the two $\max\Upsilon_{\mathrm{rcm}}$. If $\int_{\Uparrow} Q_{\mathrm{MAR}}$ is expressed as a percentage of $\int_{\Downarrow} Q_{\mathrm{MAR}}$, we find that for 2012 $\int_{\Uparrow} Q_{\mathrm{MAR}}$ corresponds to 20 % of $\int_{\Downarrow} Q_{\mathrm{MAR}}$. For the year 2017, the percentage is 3.2 % which is somewhat lower than the mean of all years (5.7 %).

The above statistics are based on Q_{MAR} alone and the question arises how relevant $\int_{\Uparrow} Q_{\mathrm{MAR}}$ is, given that simulated runoff of the two RCMs *below* IMAU-FDM $\max\Upsilon_{\mathrm{rcm}}$ are not identical. We label the area below $\max\Upsilon_{\mathrm{rcm}}$ as the "common runoff
280 area" and we find that over this area, MAR simulates 5.3±7.1 % (mean±1 std. dev.) more runoff than IMAU-FDM. This means that along the K-transect, and during normal melt seasons, the differences in RCM runoff caused by the diverging $\max\Upsilon_{\mathrm{rcm}}$ are similar to the differences in runoff over the common runoff area. In extraordinary melt season such as 2012 and 2019, however, the influence of the differing $\max\Upsilon_{\mathrm{rcm}}$ clearly exceeds the differences in RCM runoff over the common runoff area: In 2012, total MAR runoff along the K-transect exceeds IMAU-FDM by 29 %, out of which three quarters are due to MAR
285 runoff between the two Υ_{rcm}; in 2019, the difference in total runoff is 16 % out of which almost four fifths are due to different Υ_{rcm}.

5 Discussion

We compared modelled and remotely sensed runoff limits on the Greenland Ice Sheet regardless of fundamental differences between runoff processes detected from remote sensing and their simulations. Optical satellite imagery primarily detects *lat-*
290 *eral* runoff, visible in slush fields and meltwater streams at the surface; sub-surface runoff cannot be sensed. In contrast, current RCMs simulate runoff through *vertical* percolation alone; lateral flow cannot be simulated. However, we consider the comparison valid and valuable because (i) RCM simulated runoff should be similar to actual runoff quantities. Hence, RCM runoff has the purpose of mimicking the actual, strongly lateral, process. It should thus be tested whether the mimicking approximates the effects of the actual hydrological processes. (ii) The remotely sensed visible runoff limit approximates the actual (invisible)
295 runoff limit reasonably well at the peak of the melt season (Holmes, 1955; Clerx et al., 2022; Tedstone and Machguth, 2022). (iii) We observe the most remarkable differences not between Υ_{obs} and Υ_{rcm}, but between the two Υ_{rcm}.

5.1 Comparing MODIS and simulated runoff limits

Overall, we observe a relationship between $\max\Upsilon_{\mathrm{obs}}$ and $\max\Upsilon_{\mathrm{rcm}}$ that is in broad agreement to Ryan et al. (2019) who compared *snow lines* simulated by the two RCMs and observed from remote sensing (cf. Fig. 4 herein and Fig. 5b in Ryan et al., 2019): Runoff limits simulated by MAR are often high, but differences between melt seasons are in qualitative agreement with MODIS observations. The quality of the agreement depends on the region (cf. Fig. 4a and b). On average, IMAU-FDM $\max\Upsilon_{\mathrm{rcm}}$ fall below MODIS and variability from year to year appears suppressed.

On the scale of individual melt seasons, daily MAR data show strong drops in Υ_{rcm} during cold spells (Fig. 2). IMAU-FDM shows only moderate drops but the smoother curve is due to the coarser 10-day temporal resolution of the data. Sudden drops are not present in MODIS Υ_{obs}, which indicates that RCM vertical routing of meltwater through a 21 or up to 70 m thick firn layer is much faster than the actual runoff. In slush fields and streams water can flow along the surface for tens of kilometers (Holmes, 1955; Poinar et al., 2015; Yang et al., 2021), at speeds of a few meters per hours in slush (Clerx et al., 2022) or a few kilometers per hour in surface streams (Gleason et al., 2016). Holmes (1955) also describes that it took about two weeks after the end of melting before streams ran dry and were frozen over. The ice sheet surface hydrology has substantial inertia that is difficult to approximate by vertical routing alone.

The RCMs' lack of inertia is also evident in simulated firn evolution. Observations since 2012 at the KAN_U site show that, unlike the IMAU-FDM simulation, the ice slab is not getting buried. Instead, the depth of its surface remained roughly constant (Fig. 8). The ice slabs are of very low permeability which causes meltwater to pond in slush at their surface (Clerx et al., 2022) and to refreeze partially, over the course of a melt season, as superimposed ice (MacFerrin et al., 2019; Rennermalm et al., 2021). This feedback mechanism, by which ice slabs thicken, is challenging to mimic through a relatively instantaneous bucket scheme. In particular, both RCMs do not permit any slush formation and even thick ice layers must remain "permeable" for meltwater to be routed vertically.

We find that $\max\Upsilon_{\mathrm{rcm}}$ in RACMO 1 km are somewhat higher than for IMAU-FDM, which is either an effect of downscaling and bias correction or due to differences between the RACMO and IMAU-FDM firn models. While we cannot determine which of these two potential causes is more important, we note that there remain substantial differences between $\max\Upsilon_{\mathrm{rcm}}$ in MAR and RACMO 1 km. Furthermore, RACMO 1 km exhibits the same reduced temporal variability of $\max\Upsilon_{\mathrm{rcm}}$ as IMAU-FDM. For the remainder of the discussion, we focus on IMAU-FDM to establish which model parameterizations are the main cause of the differences in $\max\Upsilon_{\mathrm{rcm}}$ between MAR and the RACMO family of models. Identifying the root causes in the physical and empirical parameterizations, and eventually improving model physics, would allow strengthening the reliability of RCM simulated future scenarios.

5.2 Why do simulated runoff limits differ?

We argue that differences in the implementations of the bucket-scheme are the main cause of the deviations. In IMAU-FDM the uppermost elevation of fully icy firn roughly coincides with $\max\Upsilon_{\mathrm{rcm}}$ (Fig. 7). Downward routing in IMAU-FDM is instantaneous and water is only retained where pore space is available and the irreducible water saturation has not yet been

330 reached. This means in the absence of pore space, even moderate amounts of melt will run off and explains why in moderate melt years $\max\Upsilon_{\mathrm{rcm}}$ does not drop substantially below the elevation of depleted firn. In extreme melt years there is substantial melt in the IMAU-FDM firn area. However, water cannot run off because it percolates to depth and refreezes in the porous firn, as indicated by the strong firn warming in 2012 (Fig. A3). Refreezing potential in IMAU-FDM firn is large due to (i) the relatively low firn temperatures and (ii) because the firn layer in IMAU-FDM is thick (up to 70 m) and offers potentially large

335 amounts of firn air content in which meltwater can refreeze.

RACMO furthermore shows a pronounced step change in surface albedo in 2012 which roughly coincides with the runoff limit during that summer. The higher albedo above that step change reduces melt and also the likelihood of meltwater perco-lating to the bottom of the firn where it would run off. A possible reason for the step change might be that in 2012 the RACMO ELA coincides with the runoff limit. RACMO uses different albedo parameterization for snow/firn on the one hand and bare

340 ice on the other. The bare ice albedo is prescribed based on MODIS imagery (see Section 3.2.2). Above the ELA, where there is always snow/firn at the surface, the albedo is calculated independently of any MODIS data.

In MAR, runoff occurs from areas of porous firn (Fig. 7). The main reason for this is the parameterization which states that $1/3$ of meltwater reaching an ice lens runs off immediately. The remaining $2/3$ are routed further to depth. The parameterization was introduced to address lateral runoff of meltwater after ponding on top of the ice slabs (Clerx et al., 2022, in review).

345 However, the same parameterization is also responsible for MAR $\max\Upsilon_{\mathrm{rcm}}$ being very high and fluctuating strongly between years. It appears the approach needs further calibration against measurements in order to better mimic the effects of ice slabs.

A secondary reasons for MAR's higher $\max\Upsilon_{\mathrm{rcm}}$ are firn temperatures close to $0\,^\circ\mathrm{C}$ in the upper runoff area (Fig. A3). Consequently, percolating meltwater cannot refreeze and runs off. The available firn temperature measurements along the K-transect agree better with the colder temperatures simulated by IMAU-FDM (Fig. A4). However, RCM simulated firn tem-

350 peratures are sensitive to variations in firn pore space at low elevation firn sites (Langen et al., 2017; Vandecrux et al., 2024) and simulated firn temperatures can vary between adjacent grid cells (Fig. A3). Where pore space is available, water refreezes and releases latent heat; where no pore space exists, a bucket scheme routes the water to depth without releasing latent heat (cf. MAR firn density in Fig. 7 to MAR firn temperatures in Fig. A3).

A third reason for the relatively high MAR runoff limits is the thickness of the simulated firn pack. MAR's firn layer is only

355 21 m thick which, compared to IMAU-FDM, provides a lower potential for firn air or cold content and thus reduces the firn's retention potential.

5.3 Simulated runoff limits influence total runoff

We find that in intense melt years, MAR simulates up to 29 % more runoff than IMAU-FDM along the K-Transect. As the primary cause we identify the discrepancies between the two $\max\Upsilon_{\mathrm{rcm}}$. This is surprising as RCM simulated runoff is clearly

360 larger in the ablation area than at the comparably high elevations near the $\max\Upsilon_{\mathrm{rcm}}$ (Fig. 5e and f). However, MAR $\max\Upsilon_{\mathrm{rcm}}$ is always located further inland than IMAU-FDM $\max\Upsilon_{\mathrm{rcm}}$ and in the year 2012, the distance between the two runoff limits reaches ∼75 km (Fig. 5a). While MAR runoff between the two runoff limits is on average modest and indeed small compared to runoff over the RCM's common runoff area (Fig. 5e), the considerable distance causes total runoff between the two $\max\Upsilon_{\mathrm{rcm}}$

to become rather large. In melt seasons of intermediate intensity, MAR and IMAU-FDM $\max\Upsilon_{\mathrm{rcm}}$ are located closer to each other (Fig. 5b) and total runoff between them is relatively small.

The ice sheet hypsometry plays an important role in the aforementioned effect. As the ice sheet surface becomes increasingly flatter towards higher elevations, elevation differences between the two $\max\Upsilon_{\mathrm{rcm}}$ gain a larger effect in strong melt years. Under such conditions, MAR's $\max\Upsilon_{\mathrm{rcm}}$ is located at elevations where the surface slope is shallow, which increases the horizontal distance between the two $\max\Upsilon_{\mathrm{rcm}}$ (e.g. Figs. 5a and b). The runoff area simulated by MAR therefore grows substantially, unlike IMAU-FDM, whose runoff limit is insensitive to strong melting.

Although 2012 and 2019 appear as outliers when compared to most other melt seasons, the trend towards larger differences in strong melt seasons is considered valid and a logical consequence of IMAU-FDM $\max\Upsilon_{\mathrm{rcm}}$ varying weakly with melt intensity while MAR $\max\Upsilon_{\mathrm{rcm}}$ fluctuates strongly. This causes differences in runoff to grow as a result of increasing melt season intensity.

The relationship shown in Fig. 9 is only confirmed for the K-transect, which is located where differences in $\max\Upsilon_{\mathrm{rcm}}$ are at their maximum (Fig. 3). Potentially, the impact of the different $\max\Upsilon_{\mathrm{rcm}}$ on total runoff is smaller elsewhere on the ice sheet. However, Tedstone and Machguth (2022) found that 1985-2020 MAR and RACMO simulated cumulative runoff above a certain reference elevation differ by a factor of two. Their study is not fully comparable as they used a different versions of MAR and RACMO instead of IMAU-FDM. Their reference elevation is the Landsat derived mean $\max\Upsilon_{\mathrm{rcm}}$ 1985-1992, while here we calculate the difference in runoff directly based on the two Υ_{rcm}, independent of remote sensing data. Nevertheless, Tedstone and Machguth (2022) confirm substantial differences in RCM simulated runoff from a melting firn area.

Melting will intensify under continued warming, and the conditions under which the two RCMs differ the most will occur more commonly. As both models demonstrate strengths and weaknesses in reproducing MODIS Υ_{obs} and $\max\Upsilon_{\mathrm{obs}}$, it is unknown which simulates total runoff more accurately. This means uncertainty in future Greenland surface mass balance will grow with continued warming. This affects uncertainty in modelled sea level rise contribution.

6 Conclusions

We developed an improved method to detect visible runoff limits from MODIS and compared the results to modelled runoff limits from IMAU-FDM and MAR. We found large differences not only between remotely sensed and modelled data, but also between the two models. IMAU-FDM simulated runoff limits are on average somewhat lower than MODIS, and variability from year to year is strongly reduced. On average, MAR simulates substantially higher runoff limits than MODIS, but the magnitude of yearly fluctuations of MAR's runoff limits are similar to MODIS, except for some areas where the inter-annual variability exceeds MODIS. Both MAR and IMAU-FDM use a bucket scheme that routes water vertically through the firn and only partially mimics the strongly later water flux of the actual firn hydrology. Differences in the implementation of the bucket schemes are the main reasons for the deviations between MAR and IMAU-FDM runoff limits: (i) in MAR a fraction of the meltwater runs off when it encounters an ice layer inside the firn, (ii) the amount of pore space and cold content varies between

the two models because they simulate different firn depths, and (iii) the firn layer in MAR is warmer near the runoff limit which promotes runoff.

We compare total simulated RCM runoff along the K-transect and we find that MAR total runoff exceeds IMAU-FDM by up to 29 %. We show that in strong melt seasons MAR and IMAU-FDM runoff limits are separated by large horizontal distances,
400   which is the main reason for the difference in total runoff. Any differences in ablation area runoff, simulated by the two RCMs, are eclipsed by the amount of runoff that MAR simulates, in strong melt years, above the IMAU-FDM runoff limit. Ice sheet hypsometry is partially responsible for the large horizontal distance between the two runoff limits: the ice sheet surface slope becomes increasingly shallow with altitude and relatively small differences in the elevation of the runoff limits translate into large horizontal distances.

405   Increased melting is anticipated for the future. This means the situation where the two models diverge the most will become more frequent, simulated runoff might further diverge and uncertainty grow. We conclude that a reliable simulation of the surface mass balance in a melting firn zone is key to faithfully anticipate Greenland's future surface mass balance. Newly formed runoff areas will unfortunately play a major role in Greenland's future mass balance. Understanding of the physical processes in firn, firn hydrology and superimposed ice formation is essential to improve model performance.

410   *Code and data availability.*   The code and most data used in this manuscript are available at https://zenodo.org/doi/10.5281/zenodo.13332326. RCM data which are too volumous for the repository can be obtained directly from the authors.

Competing interests.   At least one of the (co)authors is an editor at the Cryosphere. The authors declare that they have no other competing interests.

14

Appendix A: Calculation of Υ_{obs} along flowlines

A1 Calculation along flowlines

We create polygons by (i) calculating actual flowlines which are (ii) buffered by $p_w/2$. This approach creates polygons of arbitrary shape and direction, here termed flowline-polygons. Even in complex topography, the direction of the flowline-polygons is always roughly perpendicular to the surface slope.

We chose to calculate flowlines based on surface velocity fields rather than surface slope (cf. Machguth and Huss, 2014). The advantage is a straightforward algorithm, as described in the following. We calculate flowlines following Fig. 3 in Cabral and Leedom (1993), using Greenland ice sheet surface velocity fields in x and y direction. Our algorithm starts at seed-points and then progresses downhill from gridcell to gridcell. A flowline enters a cell at a certain point along its margins and based on entry point, flow direction within the cell and location of the cell margins, the algorithm then calculates the point where the flowline leaves the cell and enters the following cell. A flowline ends when it reaches the ice sheet margin.

There are cases where flow directions of neighboring cells are conflicting and the algorithm would send the flowline immediately back to the cell where it came from. Such conflicts are solved by calculating the average flow direction of the two grid cells in question. The flow line then continues in average flow direction through one of the two cells.

Seed-points are created by first drawing a polygon that follows roughly the 2400 m a.s.l. elevation contour in the south of the ice sheet and descends towards the 1800 m a.s.l. contour in the north. Along the polygon, seed-points are created automatically every 15 km. Eventually, all flowlines are buffered by $p_w/2 = 10$ km to create flowline-polygons. Given the width of the flowline-polygons ($2p_w = 20$ km) and 15 km spacing of the seed points, a certain overlap of the polygons occurs and is wanted. More closely spaced polygons provide a higher spatial resolution of Υ_{obs} and make it easier to detect outliers. There are also cases where polygons overlap nearly completely due to confluence. The polygons are sifted manually to remove such polygons. The result is a set of 510 flowline-polygons (see Fig. 1).

A2 Accounting for background spatial variability of albedo

Our algorithm uses daily MODIS MOD10A1 albedo maps to assess spatial variability of albedo σ_α. The MODIS data record changes in α and σ_α as surface characteristics and hydrology evolve over the duration of a melt season. However, the satellite images also capture pattern in α that are persistent in space and time. Such persistent albedo features typically originate from topographic undulations or rock outcrops. Where persistent albedo features are frequent, they impact σ_α and interfere with detecting Υ_{obs}.

We calculate a Greenland-wide map of background σ_α, based on daily arrays of σ_α from before the start of the melt season. (i) From each spring of the 22 years 2000 to 2021, 20 daily arrays of σ_α are selected. (ii) We then calculate grid cell values of an initial background σ_α array as the median of up to 440 (22 years × 20 days) daily values (the actual number of data points is smaller due to frequent clouds or data issues). The large north-south extent of Greenland requires to vary the 20-day time-window across latitudes. Up to $\sim 75.5\,^\circ$N the time window are the days of year (DoY) $110 - 130$, between $\sim 75.5\,^\circ$N and $\sim 80\,^\circ$N DoY $120 - 140$, and north of $\sim 80\,^\circ$N DoY $130 - 150$. (iii) The final array of background σ_α is calculated by subtracting

15

the mean of all grid cells, calculated from the initial background σ_α array, from each grid cell. Any resulting negative values

455 are replaced by zero.

In detecting daily Υ_{obs}, the final array of background σ_α is subtracted from every daily array of σ_α. The thresholds used in the algorithm by Machguth et al. (2022) remain unchanged as the background σ_α array consists mostly (82 %) of zeros.

A3 Modified filtering for outliers

Candidates for Υ_{obs} require filtering to remove false positives (Machguth et al., 2022). We apply the same automated approach

460 in two stages but the filtering of the last valid candidates has been simplified (Section 4.4 in Machguth et al., 2022). If a suspicious last candidate is detected, then the updated algorithm searches for valid detections within a time window of ± 6 days and a circle of 75 km. The suspicious candidate is labeled invalid if it exceeds the median elevation of all nearby valid detections by >75 m. If the number of nearby valid detections is too small to calculate a median, the suspicious candidate is labeled 'valid'. The number of removed candidates remains similar under the updated filter algorithm, but there is no more risk

465 of consulting distant Υ_{obs} when evaluating reliability of candidates.

Appendix B: Additional Figures

References

Benson, C. S.: Stratigraphic Studies in the Snow and Firn of the Greenland Ice Sheet, Research Report 70, U.S. Army Snow, Ice and Permafrost Research Establishment, 1962.

470 Box, J. E., Bromwich, D. H., and Bai, L.-S.: Greenland ice sheet surface mass balance for 1991–2000: application of Polar MM5 mesoscale model and in-situ data, J. Geophys. Res., 109, D16 105, doi:10.1029/2003JD004451, 2004.

Brils, M., Kuipers Munneke, P., van de Berg, W. J., and van den Broeke, M.: Improved representation of the contemporary Greenland ice sheet firn layer by IMAU-FDM v1.2G, Geoscientific Model Development, 15, 7121–7138, https://doi.org/10.5194/gmd-15-7121-2022, 2022.

475 Brun, E., David, P., Sudul, M., and Brunot, G.: A numerical model to simulate snow-cover stratigraphy for operational avalanche forecasting, Journal of Glaciology, 38, 13–22, https://doi.org/10.3189/s0022143000009552, 1992.

Cabral, B. and Leedom, L. C.: Imaging vector fields using line integral convolution, in: Proceedings of the 20th Annual Conference on Computer Graphics and InteractiveTechniques, ACM, pp. 263–270, https://doi.org/10.1145/166117.166151, 1993.

Charalampidis, C., van As, D., Colgan, W. T., Fausto, R. S., MacFerrin, M., and Machguth, H.: Thermal tracking of meltwater retention in 480 the lower accumulation area of the Greenland ice sheet, Ann. Glaciol., 57, 1–10, https://doi.org/10.1017/aog.2016.2, 2016.

Clerx, N., Machguth, H., Tedstone, A., Jullien, N., Wever, N., Weingartner, R., and Roessler, O.: In situ measurements of meltwater flow through snow and firn in the accumulation zone of the SW Greenland ice sheet, The Cryosphere, 16, 4379–4401, https://doi.org/10.5194/tc-16-4379-2022, 2022.

Clerx, N., Machguth, H., Tedstone, A., and Van As, D.: Modelling lateral meltwater flow and superimposed iceformation atop Greenland's 485 near-surface ice slabs, Journal of Glaciology, in review.

Cogley, J., Hock, R., Rasmussen, L., Arendt, A., Bauder, A., Braithwaite, R., Jansson, P., Kaser, G., Möller, M., Nicholson, L., and Zemp, M.: Glossary of glacier mass balance and related terms, http://unesdoc.unesco.org/images/0019/001925/192525e.pdf, 2011.

Coléou, C. and Lesaffre, B.: Irreducible water saturation in snow: experimental results in a cold laboratory, Annals of Glaciology, 26, 64–68, https://doi.org/10.3189/1998aog26-1-64-68, 1998.

490 Covi, F., Hock, R., and Reijmer, C. H.: Challenges in modeling the energy balance and melt in the percolation zone of the Greenland ice sheet, Journal of Glaciology, https://doi.org/10.1017/jog.2022.54, 2022.

Delhasse, A., Kittel, C., Amory, C., Hofer, S., van As, D., S. Fausto, R., and Fettweis, X.: Brief communication: Evaluation of the near-surface climate in ERA5 over the Greenland ice sheet, The Cryosphere, 14, 957–965, https://doi.org/10.5194/tc-14-957-2020, 2020.

Fausto, R. S., van As, D., Mankoff, K. D., Vandecrux, B., Citterio, M., Ahlstrøm, A. P., Andersen, S. B., Colgan, W., Karlsson, N. B., 495 Kjeldsen, K. K., Korsgaard, N. J., Larsen, S. H., Nielsen, S., Pedersen, A. Ø., Shields, C. L., Solgaard, A. M., and Box, J. E.: Programme for Monitoring of the Greenland Ice Sheet (PROMICE) automatic weather station data, Earth Syst. Sci. Data, 13, 3819–3845, https://doi.org/10.5194/essd-13-3819-2021, 2021.

Fettweis, X., Gallée, H., Lefebre, F., and van Ypersele, J.-P.: The 1988–2003 Greenland ice sheet melt extent using passive microwave satellite data and a regional climate model, Climate Dyn., 27, 531–541, doi 10.1007/s00382-006-0150-8, 2006.

500 Fettweis, X., Hanna, E., Gallée, H., Huybrechts, P., and Erpicum, M.: Estimation of the Greenland ice sheet surface mass balance for the 20th and 21st centuries, The Cryosphere, 2, 117–129, http://www.the-cryosphere.net/2/117/2008/tc-2-117-2008.html, 2008.

Fettweis, X., Tedesco, M., van den Broeke, M., and Ettema, J.: Melting trends over the Greenland ice sheet (1958–2009) from spaceborne microwave data and regional climate models, The Cryosphere, 5, 359–375, https://doi.org/10.5194/tc-5-359-2011, 2011.

17

Fettweis, X., Franco, B., Tedesco, M., van Angelen, J. H., Lenaerts, J. T. M., van den Broeke, M. R., and Gallée, H.: Estimating the Greenland
505   ice sheet surface mass balance contribution to future sea level rise using the regional atmospheric climate model MAR, The Cryosphere,
        7, 469–489, https://doi.org/10.5194/tc-7-469-2013, 2013.

Fettweis, X., Box, J. E., Agosta, C., Amory, C., Kittel, C., Lang, C., van As, D., Machguth, H., and Gallée, H.: Reconstructions of
        the 1900–2015 Greenland ice sheet surface mass balance using the regional climate MAR model, The Cryosphere, 11, 1015–1033,
        https://doi.org/10.5194/tc-11-1015-2017, 2017.

510   Fettweis, X., Hofer, S., Krebs-Kanzow, U., Amory, C., Aoki, T., Berends, C. J., Born, A., Box, J. E., Delhasse, A., Fujita, K., Gierz, P.,
        Goelzer, H., Hanna, E., Hashimoto, A., Huybrechts, P., Kapsch, M.-L., King, M. D., Kittel, C., Lang, C., Langen, P. L., Lenaerts, J. T. M.,
        Liston, G. E., Lohmann, G., Mernild, S. H., Mikolajewicz, U., Modali, K., Mottram, R. H., Niwano, M., Noël, B., Ryan, J. C., Smith, A.,
        Streffing, J., Tedesco, M., van de Berg, W. J., van den Broeke, M., van de Wal, R. S. W., van Kampenhout, L., Wilton, D., Wouters, B.,
        Ziemen, F., and Zolles, T.: GrSMBMIP: intercomparison of the modelled 1980–2012 surface mass balance over the Greenland ice sheet,
515   The Cryosphere, 14, 3935–3958, https://doi.org/10.5194/tc-14-3935-2020, 2020.

Gallee, H. and Duynkerke, P. G.: Air-snow interactions and the surface energy and mass balance over the melting zone of west Greenland
        during the Greenland Ice Margin Experiment, J. Geophys. Res., 102, 13 813–13 824, 1997.

Gleason, C. J., Smith, L. C., Chu, V. W., Legleiter, C. J., Pitcher, L. H., Overstreet, B. T., Rennermalm, A. K., Forster, R. R., and Yang,
        K.: Characterizing supraglacial meltwater channel hydraulics on the Greenland Ice Sheet from in situ observations, Earth Surf. Process.
520   Landforms, 41, 2111–2122, https://doi.org/10.1002/esp.3977, 2016.

Greuell, W., Denby, B., van de Wal, R., and Oerlemans, J.: 10 years of mass-balance measurements along a transect near Kangerlussuaq,
        central West Greenland, J. Glaciol., 47, 157–158, 2001.

Greuell, W. B. and Knap, W. H.: Remote sensing of the albedo and detection of the slush line on the Greenland ice sheet, J. Geophys. Res.,
        105, 15 567–15 576, https://doi.org/10.1029/1999JD901162, 2000.

525   Hall, D. K. and Riggs, G. A.: MODIS/Terra Snow Cover Daily L3 Global 500m SIN Grid, Version 6, MOD10A1,
        https://doi.org/10.5067/MODIS/MOD10A1.006, 2016.

Hogan, R. J. and Bozzo, A.: A flexible and efficient radiation scheme for the ECMWF model, Journal of Advances in Modeling Earth
        Systems, 10, 1990–2008, https://doi.org/10.1029/2018ms001364, 2018.

Holmes, C. W.: Morphology and hydrology of the Mint Julep area, Southwest Greenland, in: Project Mint Julep Investigation of Smooth
530   Ice Areas of the Greenland Ice Cap, 1953; Part II Special Scientific Reports, Arctic, Desert, Tropic Information Center; Research Studies
        Institute; Air University, 1955.

How, P., Abermann, J., Ahlstrøm, A., Andersen, S., Box, J. E., Citterio, M., Colgan, W., Fausto., R., Karlsson, N., Jakobsen, J., Langley, K.,
        Larsen, S., Lund, M., Mankoff, K., Pedersen, A., Rutishauser, A., Shield, C., Solgaard, A., Van As, D., Vandecrux, B., and Wright, P.:
        PROMICE and GC-Net automated weather station data in Greenland, https://doi.org/10.22008/FK2/IW73UU, 2022.

535   IMBIE Team: Mass balance of the Antarctic ice sheet from 1992 to 2017, Nature, 558, 219–221, https://doi.org/10.1038/s41586-018-0179-y,
        2018.

IMBIE Team: Mass balance of the Greenland Ice Sheet from 1992 to 2018, Nature, pp. 233–239, https://doi.org/10.1038/s41586-019-1855-2,
        2020.

Joughin, I., Smith, B., Howat, I., and Scambos, T.: MEaSUREs Multi-year Greenland Ice Sheet Velocity Mosaic, Version 1,
540   https://doi.org/10.5067/QUA5Q9SVMSJG, 2016.

Joughin, I., Smith, B., and Howat, I.: A complete map of Greenland ice velocity derived from satellite data collected over 20 years, Journal of Glaciology, 64, 1–11, https://doi.org/10.1017/jog.2017.73, 2017.

Karlsson, N. B., Eisen, O., Dahl-Jensen, D., Freitag, J., Kipfstuhl, S., Lewis, C., T.Nielsen, L., D.Paden, J., Winter, A., and Wilhelms, F.: Accumulation Rates during1311–2011 CE in North-Central Greenland Derived from Air-Borne Radar Data, Frontiers, 4,
545   https://doi.org/10.3389/feart.2016.00097, 2016.

Kuipers Munneke, P., van den Broeke, M. R., Lenaerts, J. T. M., Flanner, M. G., Gardner, A. S., and van de Berg, W. J.: A new albedo parameterization for use in climate models over the Antarctic ice sheet, Journal of Geophysical Research, 116, https://doi.org/10.1029/2010jd015113, 2011.

Langen, P. L., Fausto, R. S., Vandecrux, B., Mottram, R. H., and Box, J. E.: Liquid Water Flow and Retention on the Greenland Ice Sheet in the
550   Regional Climate Model HIRHAM5: Local and Large-Scale Impacts, Front. Earth Sci., 4, 110, https://doi.org/10.3389/feart.2016.00110, 2017.

Lefebre, F., Fettweis, X., Gallée, H., Ypersele, J.-P. V., Marbaix, P., Greuell, W., and Calanca, P.: Evaluation of a high-resolution regional climate simulation over Greenland, Climate Dyn., 25, 99–116, 2005.

Ligtenberg, S. R. M., Helsen, M. M., and van den Broeke, M. R.: An improved semi-empirical model for the densification of Antarctic firn,
555   The Cryosphere, 5, 809–819, https://doi.org/10.5194/tc-5-809-2011, 2011.

Ligtenberg, S. R. M., Munneke, P. K., Noël, B. P. Y., and van den Broeke, M. R.: Brief communication: Improved simulation of the present-day Greenland firn layer (1960–2016), The Cryosphere, 12, 1643–1649, https://doi.org/10.5194/tc-12-1643-2018, 2018.

MacFerrin, M., Machguth, H., van As, D., Charalampidis, C., Stevens, C. M., Heilig, A., Vandecrux, B., Langen, P. L., Mottram, R., Fettweis, X., van den Broeke, M. R., Pfeffer, W. T., Moussavi, M. S., and Abdalati, W.: Rapid expansion of Greenland's low-permeability ice slabs,
560   Nature, 573, 403–407, https://doi.org/10.1038/s41586-019-1550-3, 2019.

Machguth, H. and Huss, M.: The length of the world's glaciers – a new approach for the global calculation of center lines, The Cryosphere, 8, 1741–1755, https://doi.org/10.5194/tc-8-1741-2014, 2014.

Machguth, H., MacFerrin, M., van As, D., Box, J. E., Charalampidis, C., Colgan, W., Fausto, R. S., Meijer, H. A. J., Mosley-Thompson, E., and van de Wal, R. S. W.: Greenland meltwater storage in firn limited by near-surface ice formation, Nature Climate Change, 6, 390–393,
565   https://doi.org/10.1038/nclimate2899, 2016a.

Machguth, H., Thomsen, H., Weidick, A., Ahlstrøm, A. P., Abermann, J., Andersen, M. L., Andersen, S., Bjørk, A. A., Box, J. E., Braithwaite, R. J., Bøggild, C. E., Citterio, M., Clement, P., Colgan, W., Fausto, R. S., Gleie, K., Gubler, S., Hasholt, B., Hynek, B., Knudsen, N., Larsen, S., Mernild, S., Oerlemans, J., Oerter, H., Olesen, O., Smeets, C., Steffen, K., Stober, M., Sugiyama, S., van As, D., van den Broeke, M., and van de Wal, R. S.: Greenland surface mass balance observations from the ice sheet ablation area and local glaciers, J. Glaciol., 62,
570   861–887, https://doi.org/10.1017/jog.2016.75, 2016b.

Machguth, H., Tedstone, A., and Mattea, E.: Daily variations in western Greenland slush limits, 2000 to 2021, mapped from MODIS, Journal of Glaciology, 69, 191–203, https://doi.org/10.1017/jog.2022.65, 2022.

Miège, C., Forster, R. R., Brucker, L., Koenig, L. S., Solomon, D. K., Paden, J. D., Box, J. E., Burgess, E. W., Miller, J. Z., McNerney, L., Brautigam, N., Fausto, R. S., and Gogineni, S.: Spatial extent and temporal variability of Greenland firn aquifers detected by ground and
575   airborne radars, Journal of Geophysical Research, 121, 2381–2398, https://doi.org/10.1002/2016JF003869, 2016.

Mikkelsen, A. B., Hubbard, A., MacFerrin, M., Box, J., Doyle, S., Fitzpatrick, A., Hasholt, B., Bailey, H., Lindbäck, K., and Pettersson, R.: Extraordinary runoff from the Greenland Ice Sheet in 2012 amplified by hypsometry and depleted firn-retention, The Cryosphere, 10, 1147–1159, https://doi.org/10.5194/tc-10-1147-2016, 2016.

Mohajerani, Y., Velicogna, I., and Rignot, E.: Evaluation of regional climate models using regionally optimized GRACE mascons in the Amery and Getz ice shelves basins, Antarctica, Geophysical Research Letters, 46, 13 883–13 891, https://doi.org/10.1029/2019gl084665, 2019.

Morcrette, J.-J.: Assessment of the ECMWF model cloudiness and surface radiation fields at the ARM SGP site, Monthly Weather Review, 130, 257–277, https://doi.org/10.1175/1520-0493(2002)130<0257:aotemc>2.0.co;2, 2002.

Noël, B., van de Berg, W. J., Machguth, H., Lhermitte, S., Howat, I., Fettweis, X., and van den Broeke, M.: A daily, 1-km resolution dataset of downscaled Greenland ice sheet surface mass balance (1958–2015), The Cryosphere, 10, 2361–2377, https://doi.org/10.5194/tc-10-2361-2016, 2016.

Noël, B., van de Berg, W. J., van Wessem, J. M., van Meijgaard, E., van As, D., Lenaerts, J. T. M., Lhermitte, S., Kuipers Munneke, P., Smeets, C. J. P. P., van Ulft, L. H., van de Wal, R. S. W., and van den Broeke, M. R.: Modelling the climate and surface mass balance of polar ice sheets using RACMO2 – Part 1: Greenland (1958-2016), The Cryosphere, 12, 811–831, https://doi.org/10.5194/tc-12-811-2018, 2018.

Noël, B., van de Berg, W. J., Lhermitte, S., and van den Broeke, M. R.: Rapid ablation zone expansion amplifies north Greenland mass loss, Science Advances, 5, https://doi.org/10.1126/sciadv.aaw0123, 2019.

Poinar, K., Joughin, I., Das, S. B., Behn, M. D., Lenaerts, J. T. M., and van den Broeke, M. R.: Limits to future expansion of surface-melt-enhanced ice flow into the interior of western Greenland, Geophys. Res. Lett., 42, 1800–1807, https://doi.org/10.1002/2015GL063192, 2015.

Porter, C., Morin, P., Howat, I., Noh, M.-J., Bates, B., Peterman, K., Keesey, S., Schlenk, M., Gardiner, J., Tomko, K., Willis, M., Kelleher, C., Cloutier, M., Husby, E., Foga, S., Nakamura, H., Platson, M., Wethington, M., Williamson, C., Bauer, G., Enos, J., Arnold, G., Kramer, W., Becker, P., Doshi, A., D'Souza, C., Cummens, P., Laurier, F., and Bojesen, M.: "ArcticDEM", Harvard Dataverse, V1, https://doi.org/10.7910/DVN/OHHUKH, 2018.

Rae, J. G. L., Aðalgeirsdóttir, G., Edwards, T. L., Fettweis, X., Gregory, J. M., Hewitt, H. T., Lowe, J. A., Lucas-Picher, P., Mottram, R. H., Payne, A. J., Ridley, J. K., Shannon, S. R., van de Berg, W. J., van de Wal, R. S. W., , and van den Broeke, M. R.: Greenland ice sheet surface mass balance: evaluating simulations and making projections with regional climate models, The Cryosphere, 6, 1275–1294, https://doi.org/10.5194/tc-6-1275-2012, 2012.

Rastner, P., Bolch, T., Mölg, N., Machguth, H., Le Bris, R., and Paul, F.: The first complete inventory of the local glaciers and ice caps on Greenland, The Cryosphere, 6, 1483–1495, https://doi.org/10.5194/tc-6-1483-2012, 2012.

Rennermalm, A. K., Hock, R., Covi, F., Xiao, J., Corti, G., Kingslake, J., Leidman, S. Z., Miège, C., Macferrin, M., Machguth, H., Osterberg, E., Kameda, T., and McConnell, J.: Shallow firn cores 1989–2019 in southwest Greenland's percolation zone reveal decreasing density and ice layer thickness after 2012, Journal of Glaciology, 68, 431–442, https://doi.org/10.1017/jog.2021.102, 2021.

Ryan, J. C., Smith, L. C., van As, D., Cooley, S. W., Cooper, M. G., Pitcher, L. H., and Hubbard, A.: Greenland Ice Sheet surface melt amplified by snowline migration and bare ice exposure, Science Advances, 5, eaav3738, https://doi.org/10.1126/sciadv.aav3738, 2019.

Shumskii, P. A.: Osnovy Strukturnogo Ledovedeniya, Izdatel'stvo Akademii Nauk SSSR, 1955.

Shumskii, P. A.: Principles of structural glaciology (Translated from the Russian by David Kraus), Dover Publications, New York, 1964.

Slater, T., Shepherd, A., McMillan, M., Leeson, A., Gilbert, L., Muir, A., Munneke, P. K., Noël, B., Fettweis, X., van den Broeke, M., and Briggs, K.: Increased variability in Greenland Ice Sheet runoff from satellite observations, Nature Communications, https://doi.org/10.1038/s41467-021-26229-4, 2021.

Steffen, K. and Box, J. E.: Surface climatology of the Greenland ice sheet: Greenland Climate Network 1995–1999, J. Geophys. Res., 106, 33 951–33 964, https://doi.org/10.1029/2001JD900161, 2001.

Tedstone, A. and Machguth, H.: Increasing surface runoff from Greenland's firn areas, Nature Climate Change, 12, 672–676, https://doi.org/10.1038/s41558-022-01371-z, 2022.

620 van de Berg, W. J., van den Broeke, M. R., Reijmer, C. H., and van Meijgaard, E.: Reassessment of the Antarctic surface mass balance using calibrated output of a regional atmospheric climate model, Journal of Geophysical Research: Atmospheres, 111, https://doi.org/10.1029/2005jd006495, 2006.

Van de Wal, R., Greuell, W., van den Broeke, M., Reijmer, C., and Oerlemans, J.: Surface mass-balance observations and automatic weather station data along a transect near Kangerlussuaq, west Greenland, Ann. Glaciol., 42, 311–316, 2005.

625 Van de Wal, R. S. W., Boot, W., Smeets, C. J. P. P., Snellen, H., van den Broeke, M. R., and Oerlemans, J.: Twenty-one years of mass balance observations along the K-transect, West Greenland, Earth Systems Science Data, 4, 31–35, https://doi.org/10.5194/essd-4-31-2012, 2012.

van den Broeke, M., Duynkerke, P., and Oerlemans, J.: The observed katabatic flow at the edge of the Greenland ice sheet during GIMEX-91, Global Planet. Change, 9, 3–15, https://doi.org/10.1016/0921-8181(94)90003-5, 1994.

Vandecrux, B.: Greenland ice sheet 10 m subsurface temperature compilation 1912-2022, https://doi.org/10.22008/FK2/TURMGZ, 2023.

630 Vandecrux, B., Fausto, R. S., Box, J. E., Covi, F., Hock, R., Rennermalm, A. K., Heilig, A., Abermann, J., van As, D., Bjerre, E., Fettweis, X., Smeets, P. C. J. P., Munneke, P. K., van den Broeke, M. R., Brils, M., Langen, P. L., Mottram, R., and Ahlstrøm, A. P.: Historical snow and ice temperature observations document the recent warming of the Greenland ice sheet, EGU Sphere, https://doi.org/10.5194/tc-2023-105, 2023.

Vandecrux, B., Fausto, R. S., Box, J. E., Covi, F., Hock, R., Rennermalm, A. K., Heilig, A., Abermann, J., van As, D., Bjerre, E., Fettweis,
635 X., Smeets, P. C. J. P., Kuipers Munneke, P., van den Broeke, M. R., Brils, M., Langen, P. L., Mottram, R., and Ahlstrøm, A. P.: Recent warming trends of the Greenland ice sheet documented by historical firn and ice temperature observations and machine learning, The Cryosphere, 18, 609–631, https://doi.org/10.5194/tc-18-609-2024, 2024.

Vermote, E. and Wolfe, R.: MOD09GA MODIS/Terra Surface Reflectance Daily L2G Global 1km and 500m SIN Grid V006, https://doi.org/10.5067/MODIS/MOD09GA.006, 2015.

640 Yang, K., Smith, L. C., Cooper, M. G., Pitcher, L. H., van As, D., Lu, Y., Lu, X., and Li, M.: Seasonal evolution of supraglacial lakes and rivers on the southwest Greenland ice sheet, Journal of Glaciology, pp. 1–11, https://doi.org/10.1017/jog.2021.10, 2021.

Zhang, W., Yang, K., Smith, L. C., Wang, Y., van As, D., Noël, B., Lu, Y., and Liu, J.: Pan-Greenland mapping of supraglacial rivers, lakes, and water-filled crevasses in a cool summer (2018) and a warm summer (2019), Remote Sensing of Environment, 297, 113 781, https://doi.org/10.1016/j.rse.2023.113781, 2023.
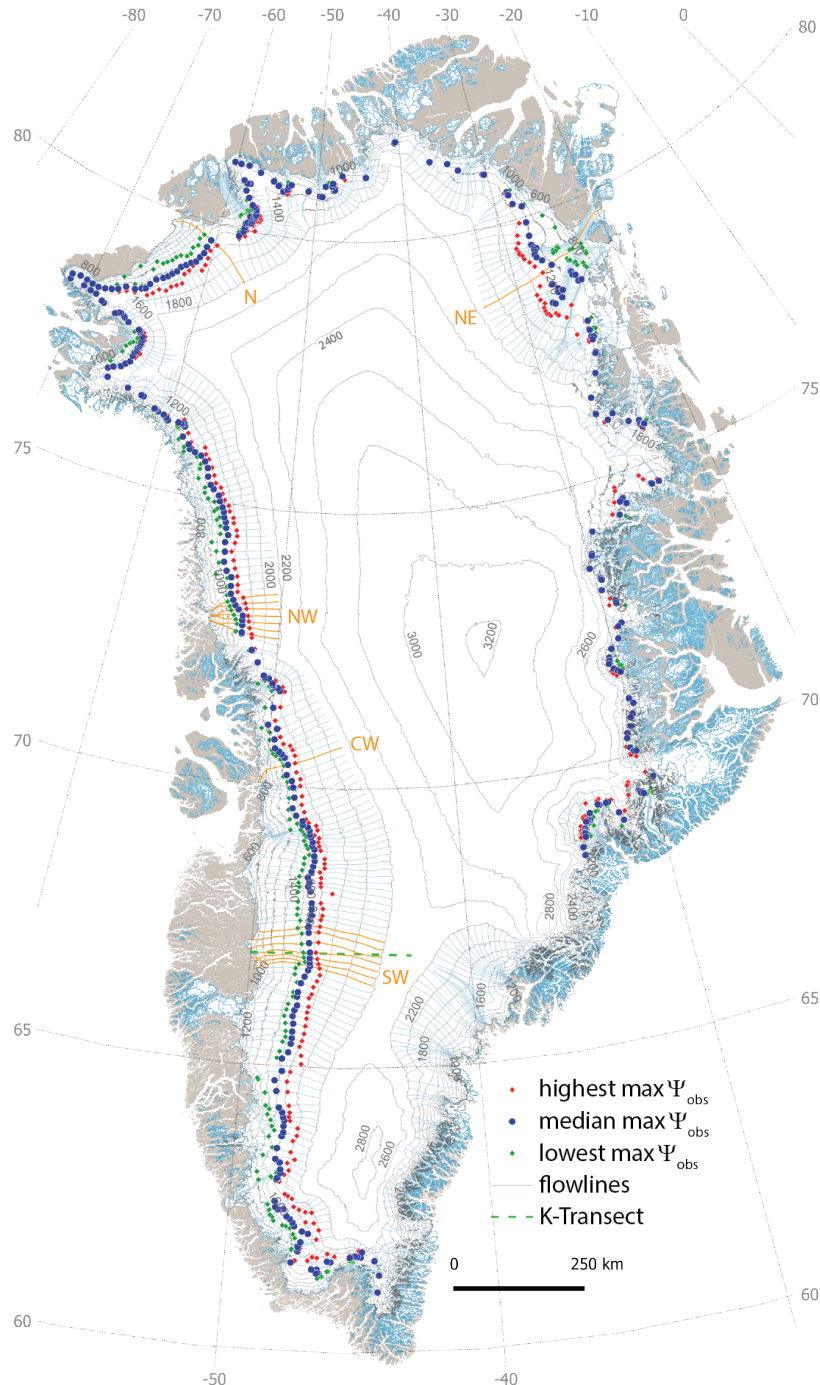
Figure 1. Median, highest and lowest of all annual MODIS $\max\Upsilon_{obs}$ for the time period 2000 to 2021. Retrievals at the east coast between $60\,^{\circ}$ to $68.4\,^{\circ}$N, where the hydrological regime is dominated by firn aquifers, have been masked. Flowlines highlighted in orange indicate the locations for which detailed results are shown in Figs. 2, 4, A1 and A2. The location of the K-transect (Figs. 5, 6 and A3) is indicated as well.
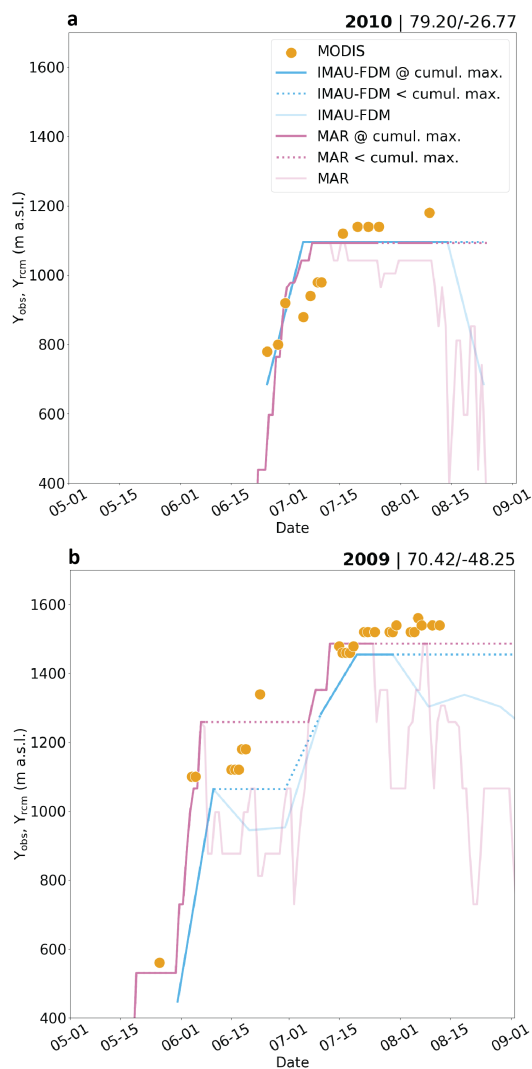
Figure 2. Evolution of Υ_{obs} and Υ_{rcm} over two selected melt seasons and flowlines. Solid lines show the cumulative maxima of the modelled runoff limits at any given point in time. The pale lines show the actual runoff limits at daily resolution for MAR and in 10-day steps for IMAU-FDM. Where the actual daily runoff limit is below the cumulative maximum, the latter is shown as a dotted lines. Subplot **a** shows data for the transect NE for the year 2010, **b** shows the transect CW for the year 2009. See Fig. 1 for the location of the two transects shown.
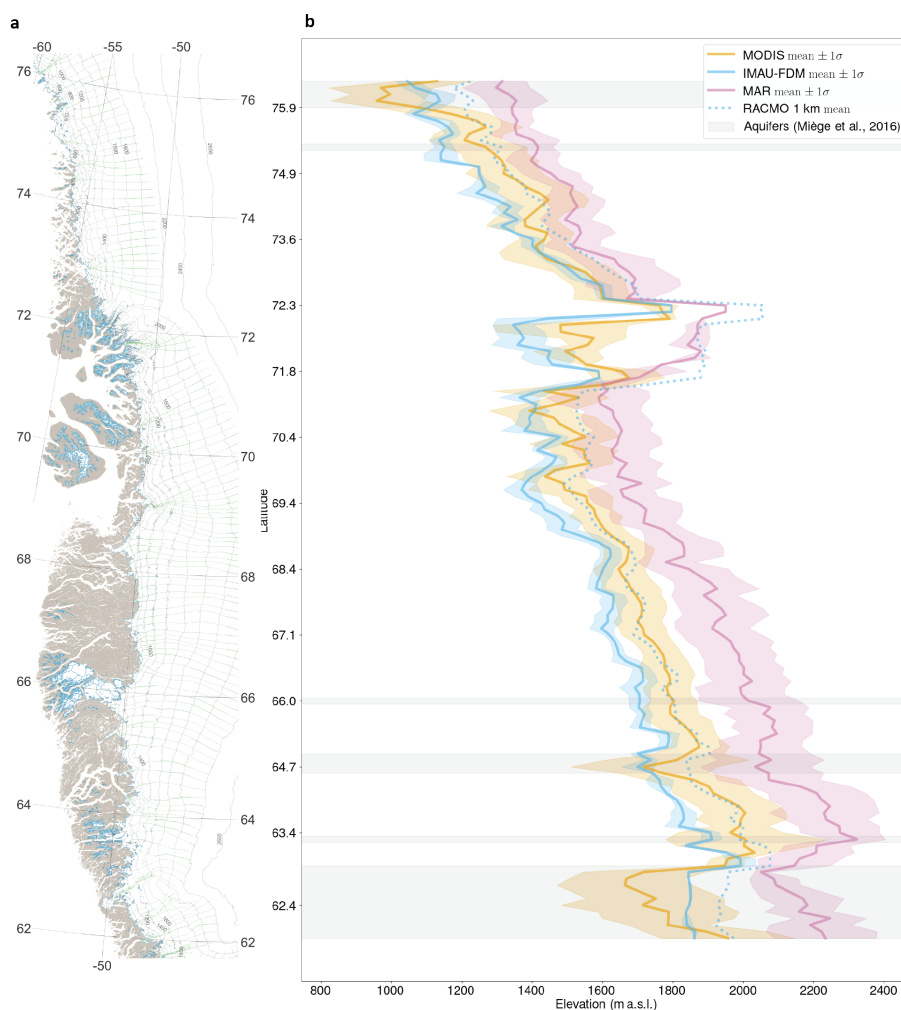
Figure 3. The western slope of the Greenland ice sheet and mean MODIS, MAR and IMAU-FDM runoff limits, averaged over the time period 2000 to 2021. **a)** Map of Greenland's west coast showing also the flowlines along which the runoff limits have been calculated. **b)** Mean and standard deviation of $\max\Upsilon_{\mathrm{obs}}$ and $\max\Upsilon_{\mathrm{rcm}}$ MODIS, MAR and IMAU-FDM for all flowlines that fall into the area shown. RACMO 1 km mean $\max\Upsilon_{\mathrm{obs}}$ are shown without standard deviation to optimize clarity of the figure. Gray shading indicates latitudes with occurrence of firn aquifers according to Miège et al. (2016).
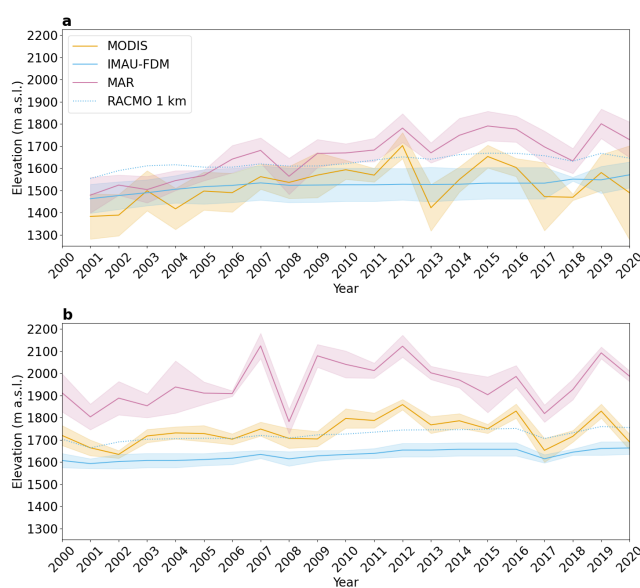
Figure 4. Annual mean of $\max\Upsilon_{\mathrm{obs}}$ and $\max\Upsilon_{\mathrm{rcm}}$ MODIS, MAR, RACMO 1 km and IMAU-FDM. **a)** Averaged over the six flowlines of region NW and **b)** averaged over the six flowlines at around the K-transect (region SW, see Fig. 1). Shading illustrates annual variability ($\pm 1\sigma$) of $\max\Upsilon_{\mathrm{obs}}$ or $\max\Upsilon_{\mathrm{rcm}}$ within the two groups of six neighboring flowlines and is omitted for RACMO 1 km to optimize clarity of the figure.
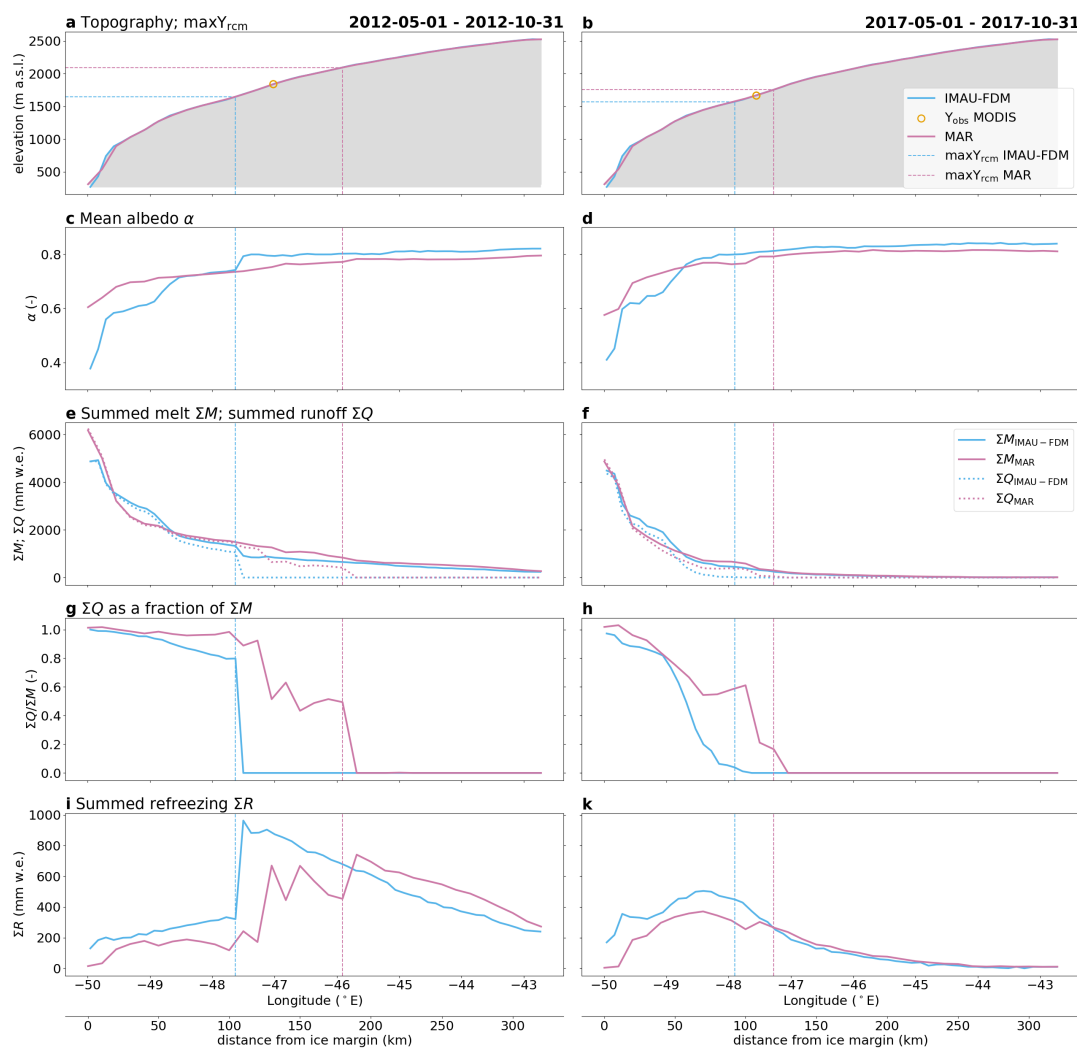
Figure 5. Comparison of RCM simulated parameters along the K-transect. The left column of subplots refers to the 2012 melt season; 2017 is to the right. The parameters shown in each row of subplots are explained in the plot titles to the left.
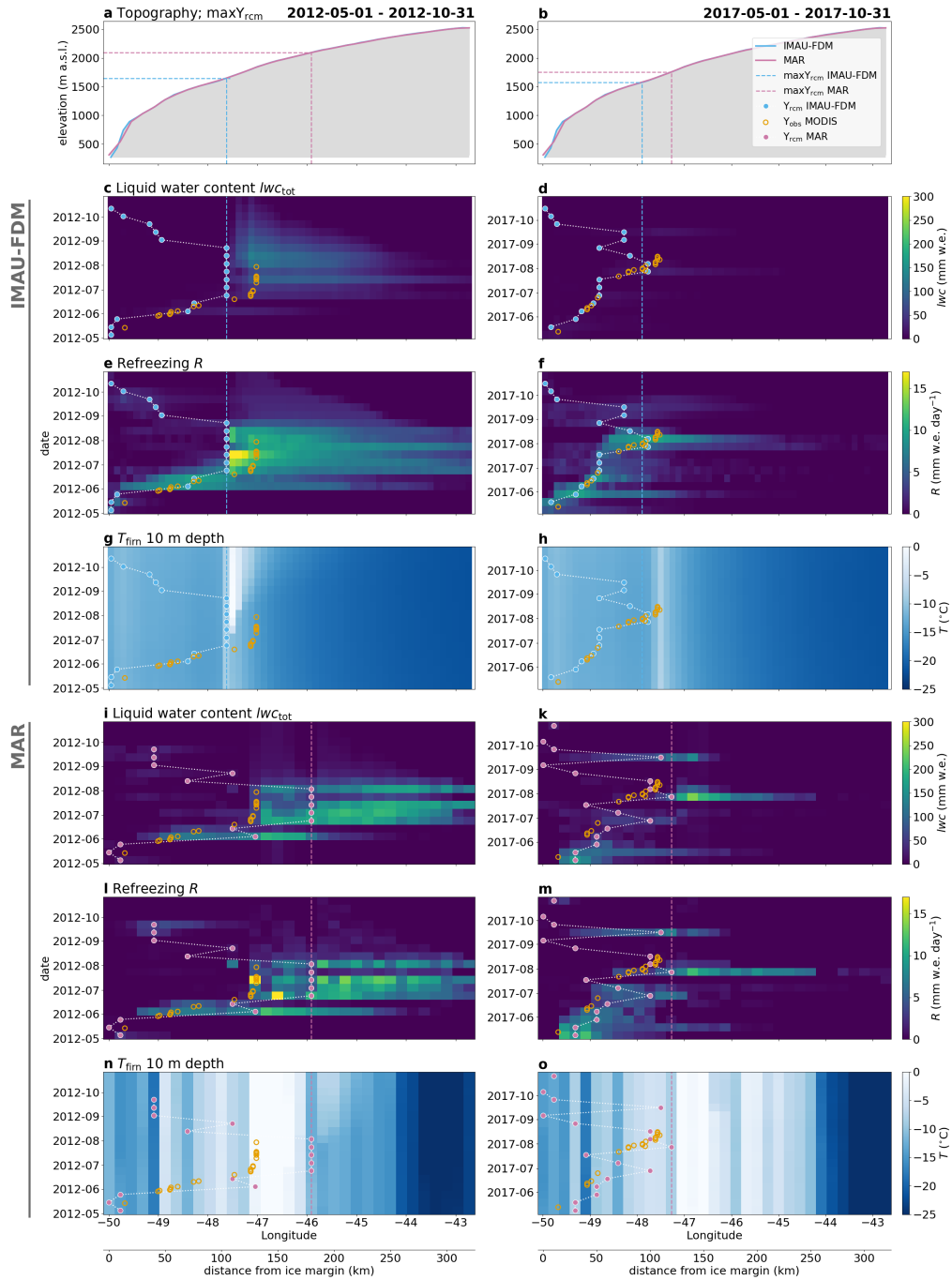
Figure 6. Comparison of IMAU-FDM (subplots **c** to **h**) and MAR (**i** to **o**) simulated parameters along the K-transect. Subplots to the left refer to the 2012 melt season; 2017 is to the right. Blue and pink dots denote RACMO and MAR simulated seasonal evolution of the runoff limit, respectively. Orange circles show MODIS-mapped seasonal evolution of the runoff limit. All heat maps are given at 10-day temporal resolution. The parameters shown in each row of subplots are explained in the plot titles to the left.
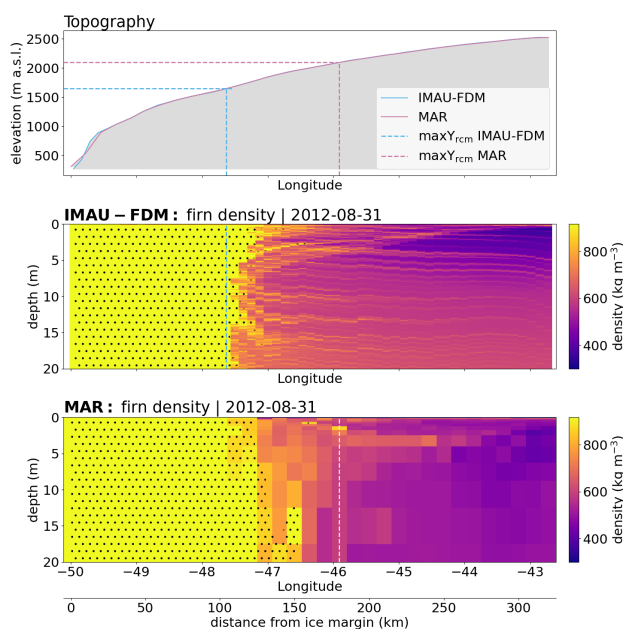
Figure 7. Comparison of RCM simulated firn structure along the K-transect and for the year 2012. Dotted areas signify depth intervals where $\rho > 830 \, \mathrm{kg \, m^{-3}}$ and exceeds pore close-of density. Runoff limits are also shown for the 2012 melt season.
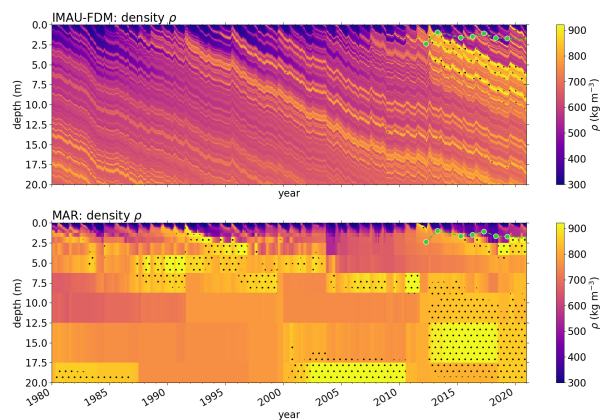
Figure 8. Evolution 1980–2020 of RCM simulated firn density ρ in the vicinity of the KAN_U site (K-transect at 1840 m a.s.l.). Dotted areas show where $\rho > 830 \, \mathrm{kg \, m^{-3}}$, i.e. exceeding pore close-off density. Green dots mark *in situ* measured depths of the top of the ice slab.
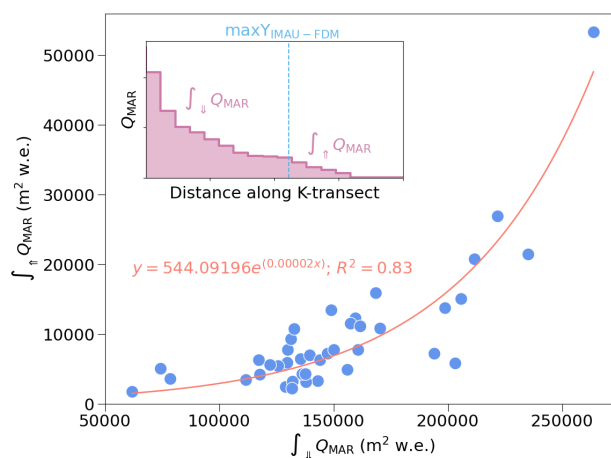
Figure 9. Regression of 1980 to 2020 MAR simulated runoff below and above the IMAU-FDM Υ_{rcm}. Every point corresponds to one year and the two runoff values for each year are integrated along parts of the K-transect as illustrated in the inset.
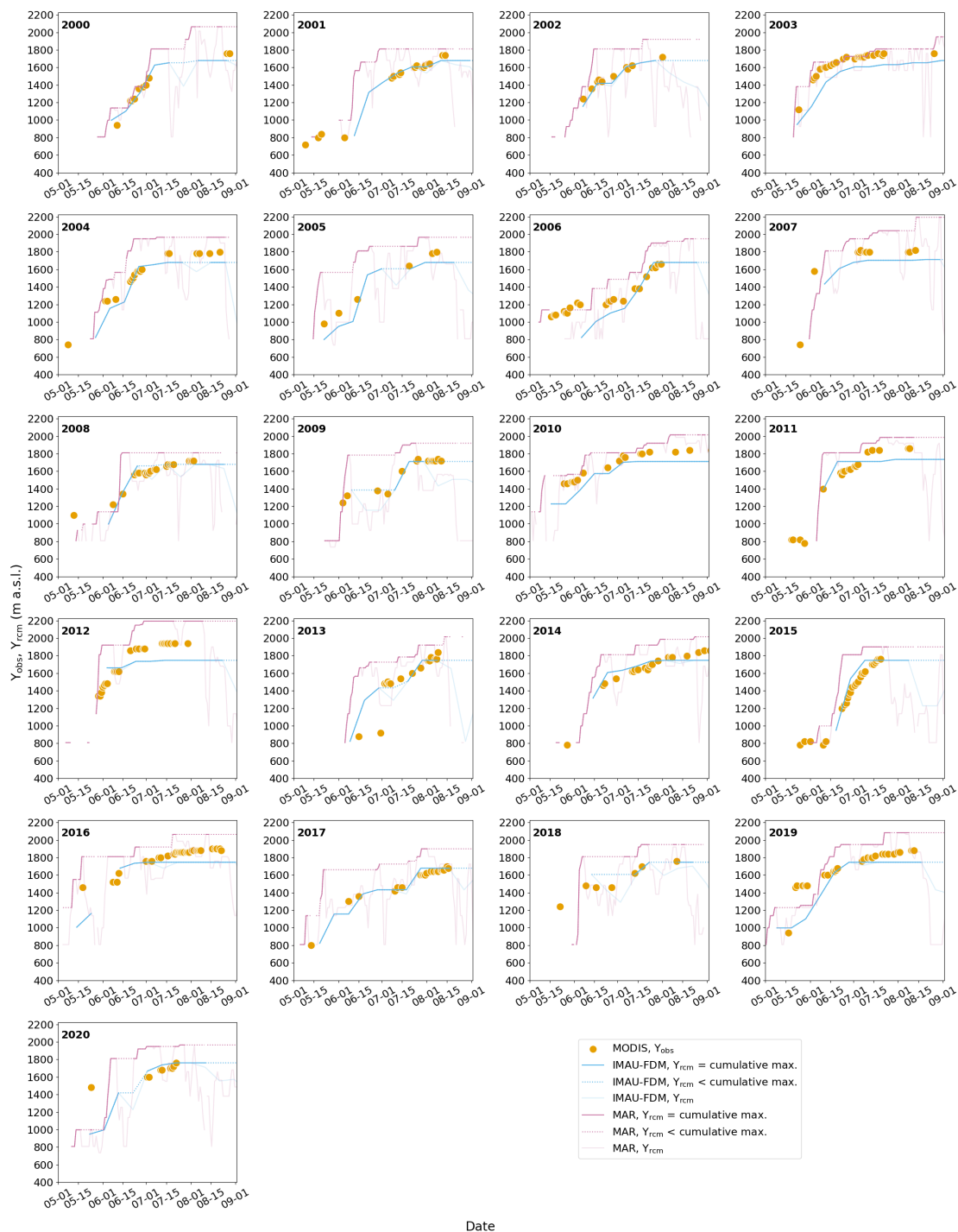
Figure A1. Seasonal evolution of Υ_{rcm} simulated by MAR and IMAU-FDM, as well as Υ_{obs} detected from MODIS. The comparison is shown for a flowline-polygon located at around 66 °N on the west coast (region SW, see Fig. 1).
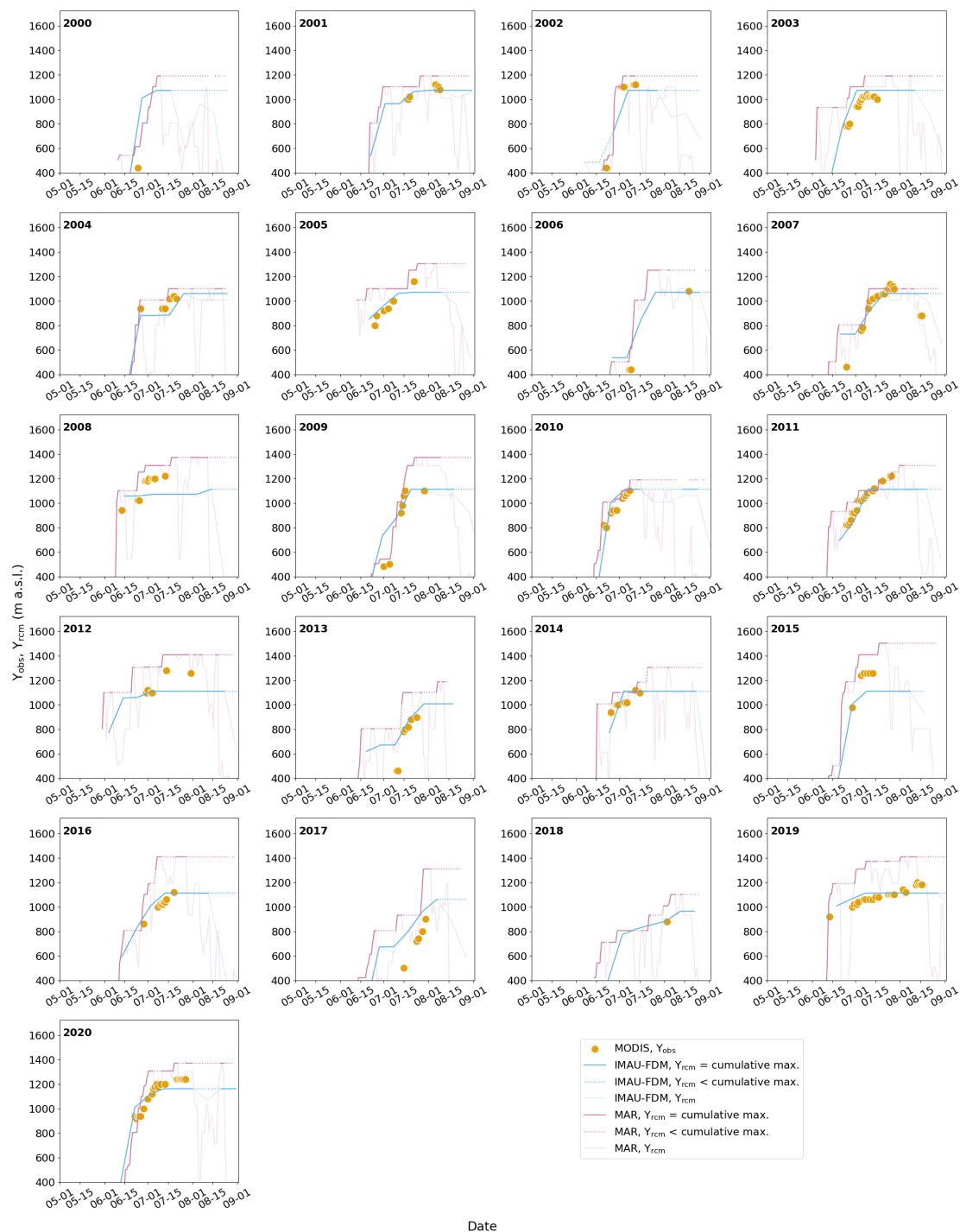
Figure A2. Seasonal evolution of Υ_{rcm} simulated by MAR and IMAU-FDM, as well as Υ_{obs} detected from MODIS. The comparison is shown for a flowline-polygon located at around $80\,^{\circ}$N (region N, see Fig. 1).
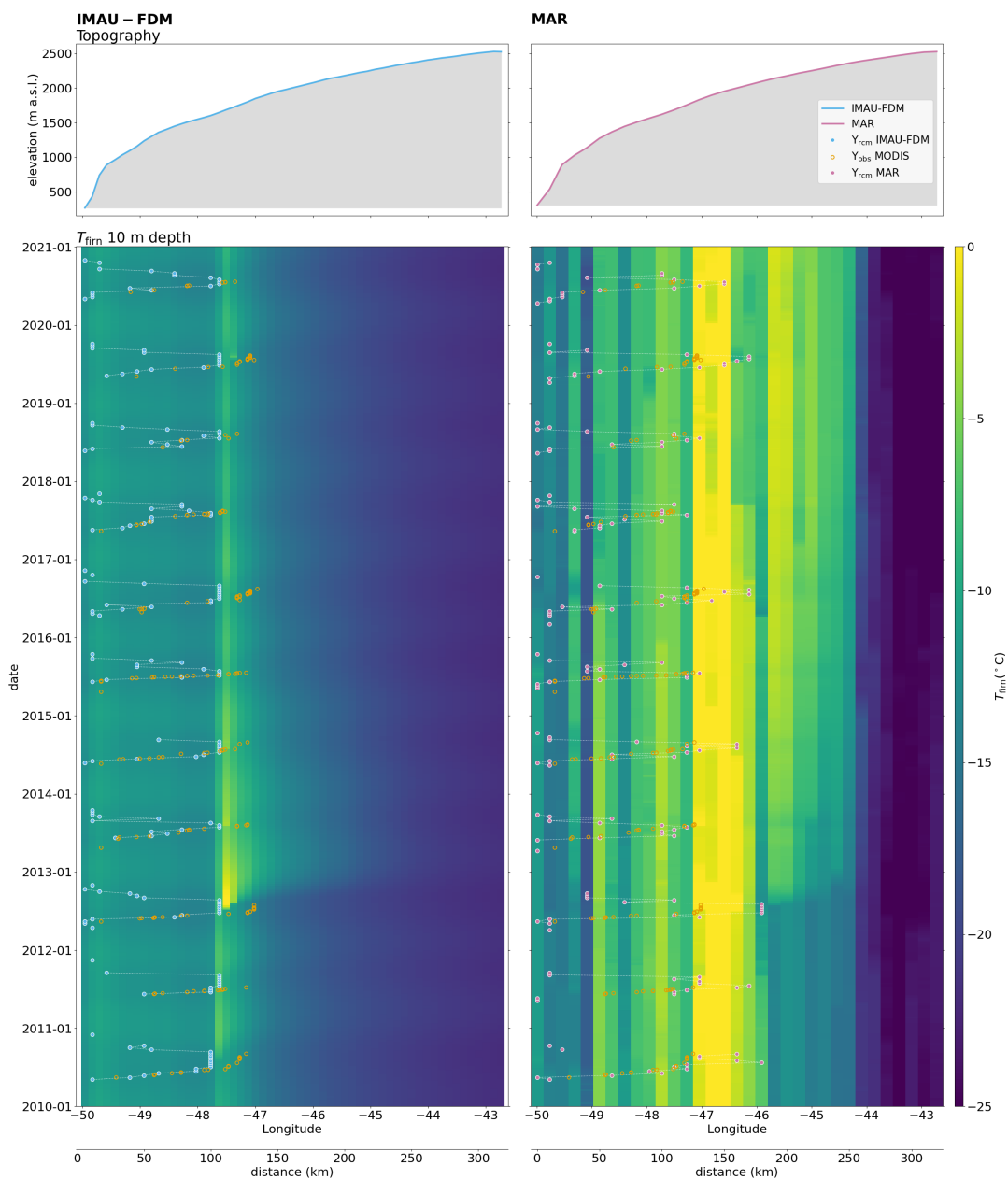
Figure A3. Comparison of RCM simulated 10 m firn temperatures along the K-transect, 2010 to 2020. Data to the left are simulated by IMAU-FDM; MAR data are shown to the right.
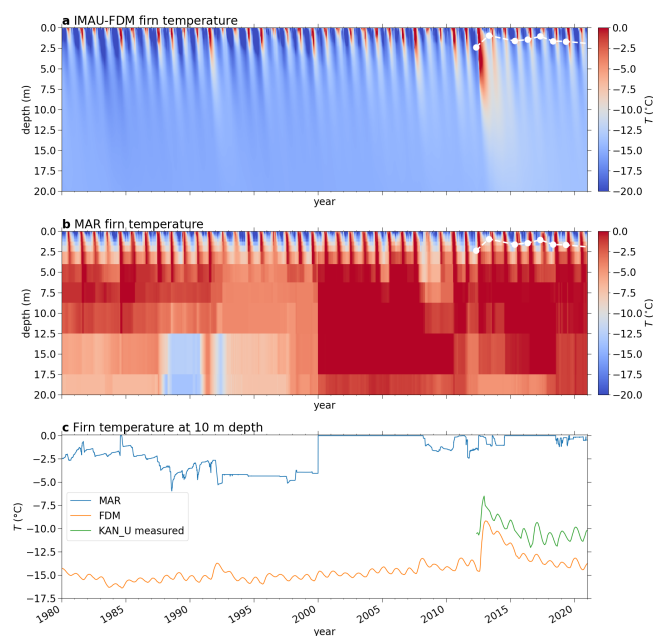
Figure A4. Comparison of RCM simulated and measured firn temperatures at the KAN_U site (1840 m a.s.l.) and for the years 1980 to 2020.
a Firn temperatures for the top 20 m simulated by FDM; **b** top 20 m firn temperatures modelled by MAR; **c** comparison of modelled and measured firn temperatures at 10 m depth (Charalampidis et al., 2016; How et al., 2022; Vandecrux et al., 2023; Vandecrux, 2023). White dots in subplots **a** and **b** denote the top of the ice slab surface according to the measurements summarized in Rennermalm et al. (2021).